Benchmarking the activity, stability, and inherent electrochemistry of amorphous molybdenum sulfide for hydrogen production

Escalera López, Daniel; Lou, Zhiheng; Rees, Neil V.

DOI:
10.1002/aenm.201802614

Document Version
Publisher's PDF, also known as Version of record

Citation for published version (Harvard):
Escalera López, D, Lou, Z & Rees, NV 2019, 'Benchmarking the activity, stability, and inherent electrochemistry of amorphous molybdenum sulfide for hydrogen production', *Advanced Energy Materials*, vol. 9, no. 8, 1802614. https://doi.org/10.1002/aenm.201802614

ADVANCED ENERGY MATERIALS
www.advenergymat.de

Benchmarking the Activity, Stability, and Inherent Electrochemistry of Amorphous Molybdenum Sulfide for Hydrogen Production

*Daniel Escalera-López, Zhiheng Lou, and Neil V. Rees**

Anodically electrodeposited amorphous molybdenum sulfide (AE-MoS_x) has attracted significant attention as a non-noble metal electrocatalyst for its high activity toward the hydrogen evolution reaction (HER). The $[Mo_3S_{13}]^{2-}$ polymer-based structure confers a high density of exposed sulfur moieties, widely regarded as the HER active sites. However, their intrinsic complexity conceals full understanding of their exact role in HER catalysis, hampering their full potential for water splitting applications. In this report, a unifying approach is adopted accounting for modifications in the inherent electrochemistry (EC), HER mechanism, and surface species to maximize the AE-MoS_x electroactivity over a broad pH region (0–10). Dramatic enhancements in HER performance by selective electrochemical cycling within reductive (overpotential shift, $\eta_{HER} \approx -350$ mV) and electro-oxidative windows ($\eta_{HER} \approx -290$ mV) are accompanied by highly stable performance in mildly acidic electrolytes. Joint analysis of X-ray photoelectron spectroscopy, Raman, and EC experiments corroborate the key role of bridging and terminal S ligands as active site generators at low pH, and reveal molybdenum oxysulfides ($Mo^{5+}O_xS_y$) to be the most active HER moiety in AE-MoS_x in mildly acidic-to-neutral environments. These findings will be extremely beneficial for future tailoring of MoS_x materials and their implementation in commercial electrolyzer technologies.

1. Introduction

Hydrogen, systematically praised as a candidate to substitute fossil fuels as an energy carrier in a carbon neutral economy, can be efficiently produced on demand and in a decentralized manner with (photo) electrochemical methods via the hydrogen evolution reaction (HER).[1–4] Despite of being the best performing HER catalysts,[5,6] noble metals such as Pt, Ir, and Pd are scarce and consequently hamper the viability of water electrolysis technologies. Hence earth-abundant materials, and notably transition metal dichalcogenides (TMDs) such as molybdenum disulfide (MoS_2), have been extensively investigated as HER electrocatalysts.[7–11]

The edge sites-driven hydrogen electroadsorption properties of TMDs[12,13] have prompted the fabrication of amorphous molybdenum sulfide materials (MoS_x) to minimize exposure of the electrocatalytically inert MoS_2 basal planes[14] for multiple applications.[15–19] A simple, yet scalable method to fabricate MoS_x has been reported by substrate-insensitive electrodeposition from a $[MoS_4]^{2-}$ precursor,[20,21] and critical properties in MoS_x materials such as film thickness,[22] morphology,[23–26] Mo:S stoichiometry,[27] as well as incorporation of dopants[28–30] or nanocomposite formation,[31–35] have been easily tuned by experimental parameters.

For long-term electrocatalytic applications, however, HER activity and stability of TMDs are paramount. In crystalline MoS_2, basal plane activation,[36–43] edge site exposure,[44–53] and metal doping/incorporation/intercalation[54–66] are the most employed strategies.

In contrast, the $[Mo_3S_{13}]^{2-}$ cluster-based polymeric structure of electrodeposited MoS_x[67] requires alternative approaches to maximize activity. In addition, the detailed HER mechanism as well as the true catalytically active sites are still under debate. Whilst pioneering studies on ambient pressure X-ray photoelectron spectroscopy (XPS) indicated the MoS_2 edge-like sites formed after MoS_3 phase transformation under in operando conditions responsible for the HER performance,[68] in situ X-ray absorption spectroscopy experiments suggested terminal S_2^{2-} ligands ($S_2^{2-}{}_{terminal}$) to be the proton acceptor sites,[69] and more recently in situ Raman spectroscopy indicated these to be the electrochemically cleaved bridging S_2^{2-} ligands ($S_2^{2-}{}_{bridging}$).[70] Another study claimed that unsaturated Mo centers formed after cathodic dissolution of $S_2^{2-}{}_{terminal}$ to be the true HER

D. Escalera-López, Z. Lou, Dr. N. V. Rees
Centre for Hydrogen and Fuel Cell Research
School of Chemical Engineering
University of Birmingham
Birmingham B15 2TT, UK
E-mail: n.rees@bham.ac.uk
D. Escalera-López
Nanoscale Physics Research Laboratory
School of Physics and Astronomy
University of Birmingham
Birmingham B15 2TT, UK
The ORCID identification number(s) for the author(s) of this article can be found under https://doi.org/10.1002/aenm.201802614.

DOI: 10.1002/aenm.201802614

active sites.[71] Strikingly, very recent in situ Raman microscopy measurements at neutral pH values suggest the active sites to stem from an internal reorganization of bridging $S_2^{2-}{}_{bridging}$ ligands to an $S_2^{2-}{}_{terminal}$ configuration yielding undercoordinated Mo—Mo sites which synergistically promoted the HER.[72]

Indeed, dramatic pH-dependent effects in crystalline MoS_2 HER performance, inherent electrochemistry and fluorescence have been reported.[73–76] Although preliminary pH studies on electrodeposited MoS_x are available,[71,77] none have proposed a unified approach to maximize the HER electrocatalysis of electrodeposited MoS_x accounting for modifications in pH-dependent surface properties. This is essential to successfully translate the efforts dedicated to MoS_x into a commercially viable TMD electrolyzer with robust long-term water splitting performances.

In this study, we have conducted a thorough analysis of the inherent electrochemical features of electrodeposited MoS_x within the pH 0–10 range, and proposed several electrochemical strategies to maximize their HER electrocatalysis. Our results not only show proof of reversible bridging $S_2^{2-}{}_{bridging}$ cleaving and irreversible terminal $S_2^{2-}{}_{terminal}$ dissolution at HER precatalytic potentials by combined analysis of the XPS and electrochemical data, but also the intimate dependence of experimental surface descriptors with the maximized/detrimental HER performances after electrochemical conditioning. Electrodeposited MoS_x films activated in the pH 3–6 region presented the highest enhancements in HER activity (≈400 mV positive shift in the HER overpotential) and extremely stable long-term performance under harsh testing conditions. Such extraordinary results are proposed to stem from the interplay between the stabilized, S-deficient molybdenum oxysulfide moieties and the modification of the HER mechanism in mildly acidic environments, providing invaluable information for the implementation of TMD-based proton-exchange membrane (PEM) electrolyzers.

2. Results and Discussion

2.1. Electrochemical Growth of Amorphous Molybdenum Sulfide

Preliminary electrochemical deposition studies were performed on Si/Ti/Au electrodes to evaluate the influence of experimental conditions (electrochemical setup, deposition parameters) on the growth of amorphous molybdenum sulfide (MoS_x) thin films. Both anodic (AE) and cathodic (CE) deposition conditions were investigated (full details are given in Section S2.1, Supporting Information), and it was found that AE-MoS_x was the preferred material due to its higher deposition efficiency (≈10 times more efficient) and reportedly improved HER properties as compared to CE-MoS_x.[27] AE-MoS_x has been therefore utilized for the remainder of this report.

2.2. AE-MoS_x Inherent Electrochemical Activity: HER Precatalytic Peaks

The AE-MoS_x enhanced activity versus CE-MoS_x has been related to the higher content of proton-accepting S sites and the multiple S moieties found in the $[Mo_3S_{13}]^{2-}$ cluster-based polymeric structure of the electrodeposit (representative schematic in **Figure 1**).[71]

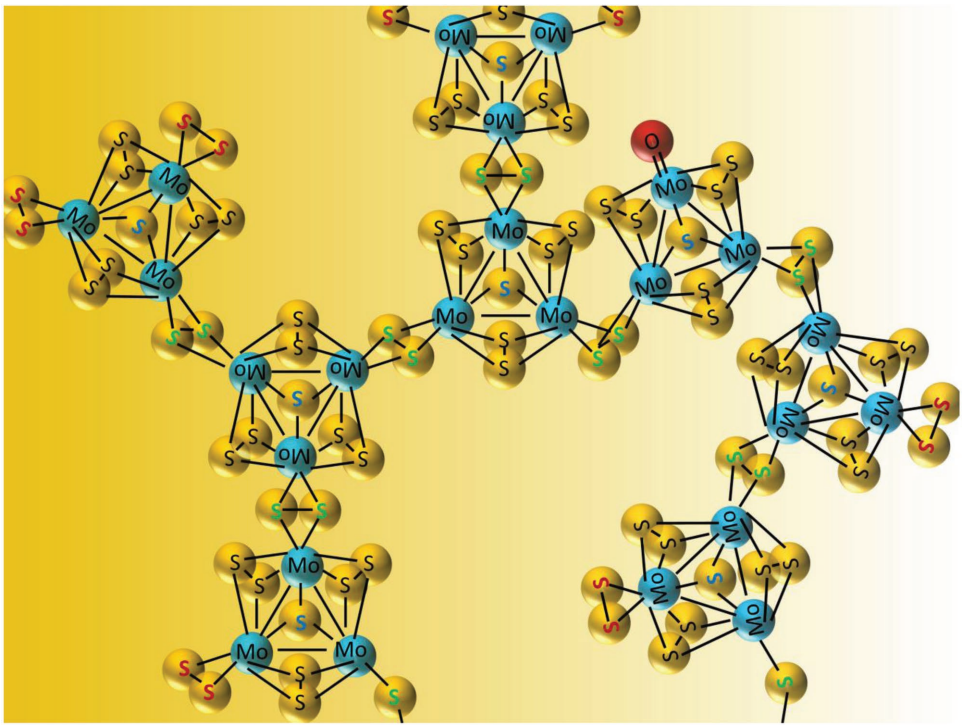

Figure 1. Schematic of the coordination polymer structure of AE-MoS_x based on the $[Mo_3S_{13}]^{2-}$ cluster unit. Sulfur ligand types labeled as follows: apical S^{2-} ($S^{2-}{}_{apical}$), blue; bridging S_2^{2-} ($S_2^{2-}{}_{bridging}$), black; terminal S_2^{2-} ($S_2^{2-}{}_{terminal}$), red; unsaturated S^{2-} ($S^{2-}{}_{unsat}$), green. S-deficient Mo-sites (AE-MoS_x structural defects, referred as $Mo^{5+}O_xS_y$) represented by Mo^{5+}=O groups.

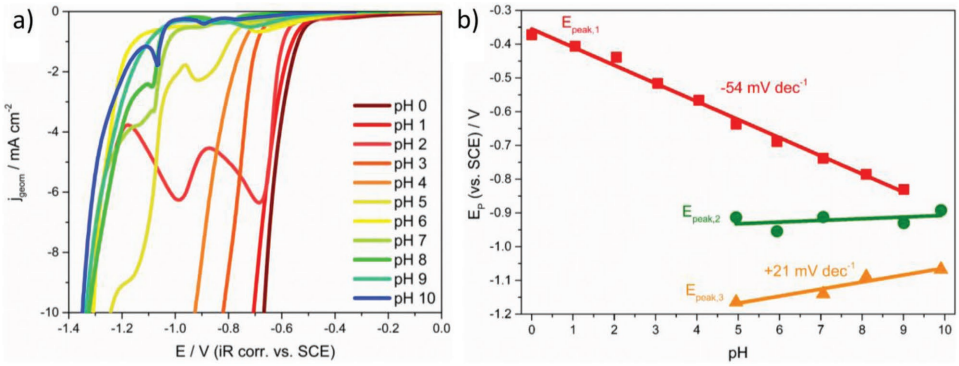

Figure 2. a) Linear sweep voltammograms recorded for pristine AE-MoS_x films (100 nm thick, catalyst loading ≈1.7×10^{-7} mol Mo cm^{-2} assuming 100% faradaic efficiency) across the 0–10 pH range by use of different buffered electrolyte solutions. b) Plotting of peak potential of the observed precatalytic redox features as a function of the buffered electrolyte pH. Scan rate: 50 mV s^{-1}.

In order to shed light on the electrochemical activity of AE-MoS_x comprehensive studies were conducted at different pHs, appropriately buffered to minimize any local pH changes that may affect the AE-MoS_x inherent electrochemistry, morphology and/or surface species (see Section S2.2 in the Supporting Information for full details). **Figure 2**a shows a compilation of the hydrogen evolution linear sweep voltammograms (LSVs) recorded for 100 nm-thick AE-MoS_x films at a voltage scan rate of 50 mV s^{-1} using different buffered electrolytes in the 0–10 pH range after *iR* compensation. The redox processes responsible for these prewaves are irreversible, appearing only on the first scan, and are involved in the so-called irreversible "activation" step which converts the S-rich AE-MoS_3 to the HER-active MoS_{2+x} phase which presents a structure/stoichiometry closer to that of CE-MoS_x.[27,78] Separate experiments on bare Si/Ti/Au electrodes confirm they are surface-related and not due to species dissolved in the buffered electrolyte solutions (see the Supporting Information).

Figure 2b shows plots of their peak potential as a function of the pH, the gradients of which can be related via the Nernst equation to the relative numbers of protons and electrons involved in the electrochemical mechanism (proton-coupled electron transfer, PCET).

For the first reduction process, $E_{peak,1}$ the gradient of −54 mV dec^{-1} is very close to the theoretical −59 mV dec^{-1} expected for redox processes involving an equivalent number of protons and electrons. Conversely, $E_{peak,2}$ and $E_{peak,3}$, found only in mildly acidic to alkaline pH conditions, present a ≈0 mV dec^{-1} and +21 mV dec^{-1} dependence, respectively. Thus, $E_{peak,2}$ involves a reduction event in which no protons are involved, whereas $E_{peak,3}$ is related to a PCET mechanism involving a two-electron : one proton ratio.

We therefore propose several potential candidates for the redox processes involved in each precatalytic feature. The in situ proof of S-S bond cleaving from $S_2^{2-}{}_{bridging}$ and $S_2^{2-}{}_{terminal}$ at potentials equivalent to that of $E_{peak,1}$ leads us to ascribe the redox process occurring at $E_{peak,1}$ to this process.[70] This involves a 2 H^+: 2e^- PCET reduction process (see reaction 1a), which would satisfy the approximate −59 mV dec^{-1} gradient experimentally observed

$$Mo^{IV}(S-S)_{br/t}\, Mo^{IV} + 2H^+ + 2e^- \rightleftharpoons 2Mo^{IV} - SH \quad (1a)$$

However, the additional evidence of the removal of $S_2^{2-}{}_{terminal}$ ligands under HER operating conditions also suggests an alternative 2 H^+: 2e^- mechanism,[71] this time leading to formation of unsaturated Mo^{4+} centers (see reaction 1b)

$$Mo^{IV}[(S-S)_t]^{2-} + 2H^+ + 2e^- \rightarrow Mo^{IV} - \blacksquare + 2\,HS^- \quad (1b)$$

While (1b) is an irreversible process, (1a) is an electrochemically reversible redox reaction. The degree of electrochemical reversibility/coexistence of these mechanisms and their implications in HER catalysis will be further investigated in Sections 2.5 and 2.6, respectively.

As for $E_{peak,2}$ and $E_{peak,3}$, their sole appearance at pH ≥ 5 might indicate that either i) the species responsible are only formed at these pH values after (1a) and (1b) occur, or ii) the species are unstable at pH ≤ 5 and consequently not present at the AE-MoS_x surface until pH ≥ 5 values are achieved. Surface composition analysis of pristine AE-MoS_x by XPS (see Figure S7, Supporting Information) suggests that the prepared films predominantly contain Mo^{4+} species, but Mo^{5+} oxysulfides and to a lesser extent MoO_3 are also present (Mo^{4+}: $Mo^{5+}O_xS_y$: Mo^{6+} XPS relative ratios 75.4: 18.6: 6.0, Figure S7a, Supporting Information), giving Mo:S ratios of 1: 2.4 ± 0.2. Previous evidence suggests that the AE-MoS_x undergoes a slow $Mo^{4+} \rightarrow Mo^{5+} \rightarrow Mo^{6+}$ transformation under atmospheric conditions[25] similar to that found in the $(NH_4)_2[MoS_4]$ precursor[79]: this could partially occur between preparation and characterization of the MoS_x thin film. The presence of $Mo^{5+}O_xS_y$ and MoO_3 at the outermost AE-MoS_x pristine surface is key as their stability is pH-dependent: MoO_3 is well known to be unstable in acidic media,[80] whereas $Mo^{5+}O_xS_y$ compounds are mostly soluble in acid unless structure-based properties confer enhanced stabilities.[81] Thus, the thermodynamically favored dissolution in acidic media eliminates their electrochemical contribution in electrolytes of pH < 5,[82] leading us to hypothesis (ii) above. We propose, analogously to a previous report,[71] $E_{peak,2}$ to be due to the electrochemically assisted reduction of $Mo^{5+}O_xS_y$ to Mo^{4+} species by reaction (2)

$$Mo^{V}O_bS_c + 1e^- \rightarrow Mo^{IV}O_bS_c \quad (2)$$

For $E_{peak,3}$, the proton-generating nature of the redox reaction involved limits the potential events occurring as Mo or S reduction events are normally proton-depleting. We herein

tentatively propose that $Mo^{4+}O_xS_y$ could further reduce at more cathodic potentials to form MoO_2 (reaction 3)

$$Mo^{IV}OS + Mo^{IV}OS_2 + 2H_2O + 2e^- \rightarrow 2MoO_2 + 3HS^- + 1H^+ \quad (3)$$

2.3. AE-MoS_x Inherent Electrochemical Activity: HER Kinetics

It is crucial to monitor changes in the HER kinetics as a function of the pH, as provides insight into the HER mechanism and hence the electrocatalytic activity. Although previous reports describe almost unaltered Tafel slope values upon incremental MoS_2 loadings,[83] layer stacking,[80] and amorphous MoS_x S:Mo stoichiometry,[78,84] the influence of the electrolyte pH is rarely documented.

We investigated this by analyzing the linear region of the η versus $\log|j_{geom}|$ plot (i.e., Tafel plot, b) of iR-compensated LSVs acquired toward hydrogen evolving potentials, over a set of independent repeated measurements at the different buffered electrolytes studied. **Figure 3**a compiles the Tafel plots of bare Si/Ti/Au (as control) substrates and AE-MoS_x thin films, the latter in the presence and absence of 1500 rpm stirring, to identify potential contributions of both substrate and mass transport in the obtained values.

A plateau in the $0 \leq pH \leq 3$ range, followed by an overall increase in the Tafel slope (b) values with pH, was found for both Si/Ti/Au substrates and AE-MoS_x films. While b seems independent on the presence of AE-MoS_x up to pH 5, Si/Ti/Au substrates exhibit slightly higher values in neutral to alkaline environments. Although the exact HER pathway on bare Au is still under debate,[85] recent investigations in acidic electrolytes have found two characteristic Tafel slope values at low ($b \approx 68 \pm 5$ mV dec^{-1}) and high current densities ($b \approx 120 \pm 2$ mV dec^{-1}) due to hydrogen surface diffusion effects,[86,87] converging to a Tafel slope of $b \approx 120$ dec^{-1} in alkaline environments.[88] AE-MoS_x films tested under stirring gave Tafel slopes with lower dispersion compared to their quiescent counterparts ($b \approx 65 \pm 10$ mV dec^{-1} in the $0 \leq pH \leq 3$ range closer to theoretical Volmer–Heyrovsky $b \approx 40$ mV dec^{-1} as reported for AE-MoS_x in acid). For further discussion of Tafel slope variations before and after stirring, see Section S2.3 (Supporting Information).

The Si/Ti/Au substrate, particularly in acidic conditions, seems to govern the experimental Tafel slopes obtained after MoS_x modification across the 0–10 pH range: supporting working electrodes of different nature[89,90] and morphology[91] yielded analogous results in previous HER experiments.

As regards the Tafel slope versus pH trend, recent studies on AE-MoS_x by Dubouis et al. using sulfuric acid in the $0 \leq pH \leq 4$ range[77] suggests that for $pH \leq 2$ the HER mechanism operated by the electroreduction of the hydronium ion ($H_3O^+ + 1e^- \rightarrow 1/2\,H_2 + H_2O$), while for $pH \geq 3$ the HER occurred via the water reduction/splitting mechanism ($H_2O + 1e^- \rightarrow 1/2\,H_2 + OH^-$).

This implies that b should be pH-insensitive for $pH \leq 2$, whereas b should increase at $pH > 3$ due to increasingly lower proton concentrations yielding the proton electroadsorption rate-limiting step (i.e., Volmer step, $b \approx 120$ mV dec^{-1}) to govern the HER performance, as (previously reported for noble metal surfaces.[92–95]). Despite using electrolytes with different spectator species and ionic strengths, this trend is also found for our AE-MoS_x results under stirring: within the $0 \leq pH \leq 2$ range, Tafel slopes are almost constant $b \approx 65 \pm 10$ mV dec^{-1}, whilst at $pH > 2$ they increase approximately linearly yielding $b \approx 120$ mV dec^{-1} at pH 5.

For neutral to alkaline pHs, however, b exceeds 120 mV dec^{-1}: since electron transfer coefficients in mildly acidic to alkaline conditions are reported to be almost pH independent,[96] mass transport limitations (i.e., proton depletion at the electrode interface) and surface species will necessarily play a role on the HER kinetics. Indeed, molybdenum oxides such as MoO_3 and MoO_2, stable in neutral to alkaline environments, exhibited Tafel slopes as high as $b \approx 160$ mV dec^{-1} and $b \approx 200$ mV dec^{-1}, respectively in 0.5 M H_2SO_4.[97] Thus, we believe that the presence such Mo_xO_y surface species at these mid-pH values with different HER active site kinetics, along with the partial exposure of the underlying Au substrate due to AE-MoS_x instability, could explain the Tafel slopes observed.

This pH-dependence on the Tafel slope, HER mechanism, and surface species consequently supports the AE-MoS_x LSVs found under stirring after iR and Nernstian compensation (Figure 3b). As found by Dubouis et al., LSVs in the $0 \leq pH \leq 2$ range fully overlap due to invariable Tafel slope and HER kinetics, whereas for $pH \geq 3$ the HER mechanism and Tafel slope modification result in nonoverlapping, negatively shifted LSVs toward higher pH values.

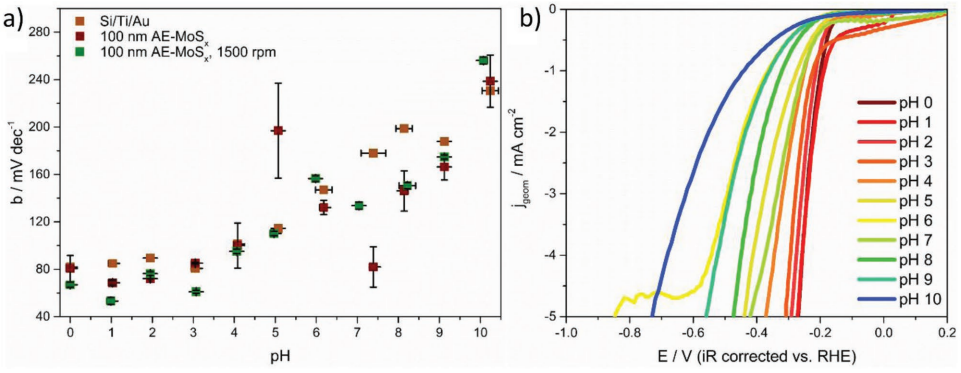

Figure 3. a) Tafel plots (η vs $\log|j_{geom}|$) for Si/Ti/Au (yellow), pristine AE-MoS_x (red), and AE-MoS_x under 1500 rpm stirring (green) across the 0–10 pH range. b) iR and Nersnstian-corrected HER linear sweep voltammograms recorded for AE-MoS_x under 1500 rpm electrolyte stirring. Scan rate: 50 mV s^{-1}.

2.4. AE-MoS_x Inherent Electrochemical Activity: Electro-Oxidation

Next, we investigated the electro-oxidative processes of the 100 nm thick AE-MoS_x films. For pristine AE-MoS_x, an LSV from ≈0 V to 1.2 V (vs SCE) reveals a broad anodic feature, in the 0.2– 1.1 V voltage range, with its peak at ≈0.7 V when tested in a 0.5 M H_2SO_4 electrolyte (**Figure 4**a). Plotting the electro-oxidation band peak potential as a function of the pH gives an experimental gradient of –27 mV dec^{-1}, which closely matches the –29.5 mV dec^{-1} theoretical Nernstian slope characteristic of a 1 H^+: 2e^- PCET electro-oxidation mechanism (Figure 4b), in agreement with literature results for crystalline MoS_2 materials ascribed to the oxidation of the Mo^{4+} moieties to Mo^{6+}.[74,98] To the best of our knowledge, our investigation is the first to experimentally support the 1 H^+: 2e^- PCET electro-oxidation mechanism for pristine AE-MoS_x(detailed discussion of the electrochemical features is provided in Section S2.4, Supporting Information).

To gain further insight on the implications of the complex electro-oxidation mechanism, ex situ Raman spectra of the electro-oxidized AE-MoS_x films were recorded (Figure S10, Supporting Information), and showed changes to several Raman-active vibrations: 1) the ν(Mo—Mo) band at ≈201 cm^{-1} sharpens and increases its relative intensity, 2) the ν(Mo—S) band at ≈358 cm^{-1} sharpens to the detriment of the remaining ν(Mo—S) bands, and undergoes a redshift to ≈354.8 cm^{-1}, 3) the out-of-plane A_{1g} mode appears at ≈404 cm^{-1}, with relative intensities higher than those found for the in-plane E^2_{1g} mode at ≈380 cm^{-1} and 4) additional Raman modes appear at ≈341 (faint), 490 (strong), and 730 (strong) cm^{-1}, respectively. This indicates that electro-oxidation irreversibly changes the morphology of the cluster-based AE-MoS_x structure: the Raman signal intensity sharpening in features 1–3) inform that the resulting structure comprises morphologies with predominance of those vibration modes. As for 4), we believe that the weakening and disappearance of ν(Mo—S) and $\nu(S—S)_{terminal}$ vibration modes, respectively, are responsible for the 341 and 490 cm^{-1} bands. Additionally, the 730 cm^{-1} band should correspond to the partial oxidation of Mo^{4+} sites, as this vibration is not far away from the one expected for Mo=O (≈880 cm^{-1}). Thus, we conclude that the 1 H^+: 2e^- PCET electro-oxidation mechanism for pristine AE-MoS_x primarily involves the disappearance of $S_2^{2-}{}_{terminal}$ and the formation of partially oxidized molybdenum sites.

To investigate the effect of reducing (i.e., HER) potentials on these electro-oxidative features, anodic voltammetry was recorded after one LSV toward HER potentials (from 0.7 to –1.2 V vs SCE, scan rate 50 mV s^{-1}) The anodic LSV showed differences compared to that performed on pristine AE-MoSx: for pH = 7 (see Figure S11, Supporting Information), two well-resolved peaks can be identified, the first ($E_{peak,I}$) at ≈–0.16 V and the second ($E_{peak,II}$) at ≈0.29 V (partially overlapped at other buffered electrolytes). These are equivalent to those previously found for AE-MoS_x being oxidatively stripped after applying a cathodic scan to HER potentials,[78,99] in stark contrast with the electro-oxidative behavior found for pristine AE-MoS_x. This suggests that electrochemical conditioning to hydrogen evolving potentials alters the electro-oxidation mechanism.

It was previously hypothesized that scanning to anodic potentials, first selectively oxidized weakly Mo-bound low XPS binding energy unsaturated S^{2-} ($S^{2-}{}_{unsat}$) and $S_2^{2-}{}_{terminal}$ to MoO_x, and eventually led to full conversion of AE-MoS_x to HER-inactive MoO_x.[78] A more recent study attributed the same voltammetric features to the irreversible oxidation of $S_2^{2-}{}_{terminal}$ and $S_2^{2-}{}_{bridging}$, respectively.[99] However, neither the pH-dependence of these reactions nor the electrochemical reversibility of reaction (1a) triggered by the initial LSV scan toward HER potentials were taken into consideration when proposing these reactions. To gather insight on these redox processes, we elucidated the pH-dependence of the post-LSV AE-MoS_x electro-oxidative features (**Figure 5**a) by plotting the electro-oxidation peak potentials versus the electrolyte pH for both $E_{peak,I}$ (Figure 5b) and $E_{peak,II}$ (Figure 5c) after Gaussian peak deconvolution. For $E_{peak,I}$, a –56 ± 4 mV dec^{-1} dependence was observed between pH 2 and pH 8. This is in excellent agreement with a 1 H^+: 1e^- (or subsequent multiples) PCET electro-oxidation mechanism. However, this does not satisfy the widely established 1 H^+: 2e^- PCET mechanism under which the irreversible electro-oxidation of MoS_2 materials to Mo^{6+} is reported to proceed, as this would give a theoretical Nernstian slope of –29.5 mV dec^{-1}.[74,98,100]

Thus, an alternative electro-oxidation event precedes the complete electrochemical oxidation of the AE-MoS_x thin film. Analysis of the voltammetric features found after cycling the post-LSV AE-MoS_x at variable voltage windows indicates that the electro-oxidation event responsible for $E_{peak,I}$ can only be found when AE-MoS_x has undergone cathodic cycling past the

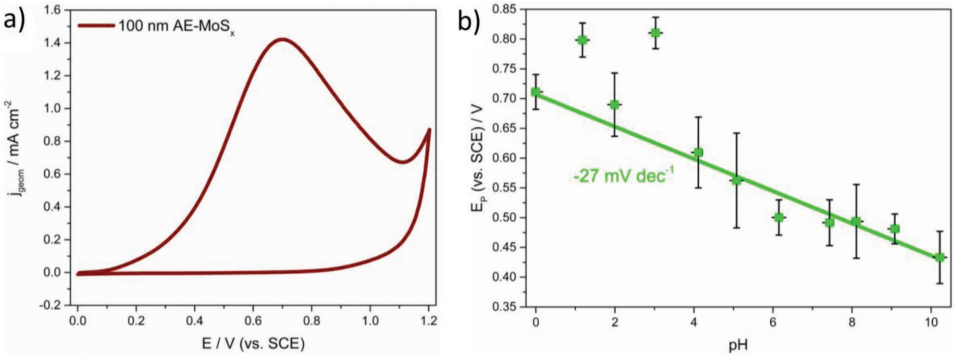

Figure 4. a) Anodic stripping voltammogram of freshly deposited AE-MoS_x films recorded from 0 to 1.2 V versus SCE in 0.5 M H_2SO_4. b) Plot of AE-MoS_x electro-oxidation peak potential versus buffered electrolyte pH showing a gradient of –27 mV dec^{-1}. Scan rate: 50 mV s^{-1}.

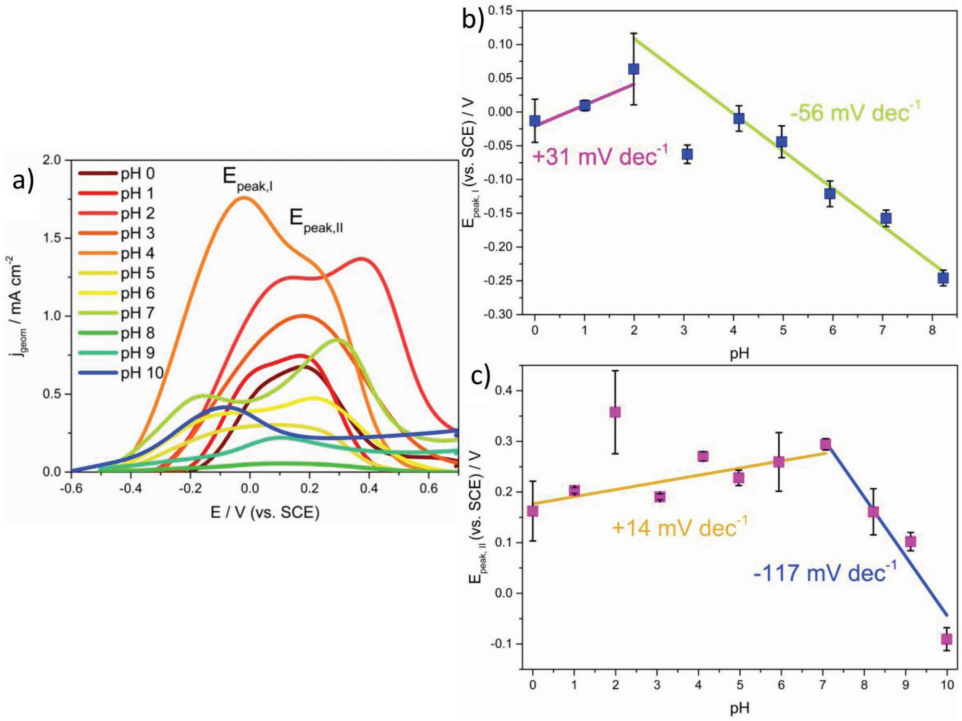

Figure 5. a) Compilation of reverse scans obtained for post-LSV AE-MoS_x films (from −1.2 to 0.7 V vs SCE) across the 0–10 pH range. Scan rate: 50 mV s^{-1}. Peak potential dependence of post-LSV AE-MoS_x electro-oxidative features labeled as b) $E_{peak,I}$ (blue) and c) $E_{peak,II}$ (magenta) as a function of the buffered electrolyte pH. Overlapped linear fits and experimental *E*–pH slopes displayed for ease of comparison.

precatalytic peak $E_{peak,1}$ (Figure S12, Supporting Information). Given the electrochemical reversibility of reaction (1a), we preliminarily suggest the electro-oxidation event $E_{peak,I}$ to be the reinstatement of the previously cleaved S—S bond in $S_2^{2-}{}_{bridging}$ and/or $S_2^{2-}{}_{terminal}$ (2 H^+: 2e^- PCET mechanism).

$$2Mo^{IV}-SH \rightleftharpoons Mo^{IV}(S-S)_{br/t}\,Mo^{IV} + 2H^+ + 2e^- \quad (4a)$$

However, the partial corrosion of the previously cleaved $S_2^{2-}{}_{bridging}$ and/or $S_2^{2-}{}_{terminal}$ sites giving MoO_2 also satisfies a close-to 1 H^+: 1e^- PCET electro-oxidation mechanism, and thus cannot be discarded.

$$Mo^{IV}-SH+6H_2O \rightarrow MoO_2 + HSO_4^- + 12H^+ + 11e^- \quad \text{(acidic pH)}$$
$$Mo^{IV}-SH+6H_2O \rightarrow MoO_2 + SO_4^{2-} + 13H^+ + 11e^- \quad \text{(neutral pH)} \quad (4b)$$

As for $E_{peak,II}$, a clear −117 ± 17 mV dec^{-1} gradient is found at neutral to alkaline pHs (7 ≤ pH ≤ 10). This satisfies a 2 H^+: 1e^- PCET mechanism: based on the thermodynamic instability seen for Mo species at positive potentials in alkaline environments,[82] we suggest the electro-oxidation of MoO_2 to the soluble MoO_4^{2-} anion to be the reaction taking place.

$$MoO_2 + 2H_2O \rightarrow \frac{1}{2}MoO_4^{2-} + 4H^+ + 2e^- \quad (5)$$

In acidic pH, $E_{peak,II}$ presents a slightly positive gradient of +14 ± 5 mV dec^{-1}. This clearly deviates from the 1 H^+: 2e^- PCET mechanism generally ascribed to MoS_2 electrodissolution, and would theoretically imply a 1 proton-depleting, 3 electron-generating PCET mechanism. This informs of a complex electro-oxidation mechanism which cannot be unambiguously described by one specific redox process. The most likely final electro-oxidation products are, according to thermodynamic stability, the acid-unstable MoO_3 (pH ≤ 1) and the solution-soluble $HMoO_4^-$ (1 ≤ pH ≤ 7).[82,101]

2.5. AE-MoS_x Inherent Electrochemical Activity: Electrochemical Conditioning

Having in mind the inherent electrochemical features found for AE-MoS_x, we proceeded to evaluate the impact of several voltammetric pretreatments on pristine thin films. These not only intend to identify an optimal activation step to maximize the AE-MoS_x thin film HER activities, but also to corroborate the redox mechanisms proposed previously. For such purpose, a combined use of electrochemical techniques, ex situ Raman and ex situ XPS measurements were used to correlate positive/negative electrocatalytic effects with modifications in surface morphology and/or species.

Multiple activation pretreatments can be chosen by tuning the electrochemical parameters: in our study cyclic voltammetry is chosen over potentiostatic preconditioning procedures because of the need to monitor any electrochemical modifications of the redox features during preconditioning. Although AE-MoS_x operate in reductive potentials under HER conditions, ex situ XPS acquired after electrochemical conditioning will enable to correlate generated/electrodissolved surface

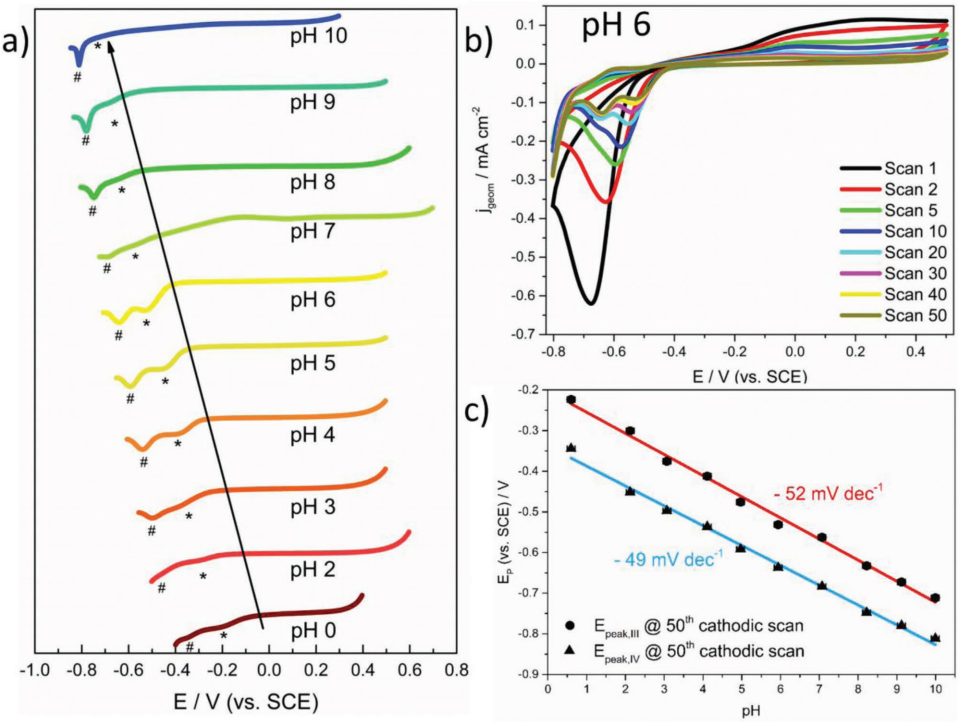

Figure 6. a) Compilation of the 50th cathodic scans recorded during the oxidative-reductive electrochemical conditioning on pristine AE-MoS_x films across the 0–10 pH range. b) Representative voltammograms obtained for AE-MoS_x films during oxidative-reductive electrochemical conditioning in a pH 6 buffered electrolyte. c) Peak potential dependence of post-LSV AE-MoS_x HER precatalytic features $E_{peak,III}$ (●, * in Figure 9a) and $E_{peak,IV}$ (▲, # in Figure 9a) as a function of the buffered electrolyte pH. Scan rate: 50 mV s^{-1}.

species and their immediate impact to the HER, which would be misguidedly ascribed if samples were to be measured after HER operation due to irreversible precatalytic redox processes as previously mentioned. Conditioning procedures considered were: reductive, oxidative and reductive-oxidative (for further details, see Section 4 and Section S2.5 in the Supporting Information). For perspective purposes, a compilation of the electrochemical performance of AE-MoS_x thin films with respect to other MoS_2-based HER catalysts is shown in Table S1 (Supporting Information).

For the electro-oxidation treatment (Figure S12a, Supporting Information), no electro-oxidative peaks are observed, but these peaks can be found for both oxidative-reductive treatments (Figures S12c,d, Supporting Information). This suggests that the species responsible for the electro-oxidation features $E_{peak,I}$ and $E_{peak,II}$ only arise after the AE-MoS_x thin films have been previously cycled past the precatalytic wave $E_{peak,1}$ at cathodic potentials. Thus, we believe that the cathodic prewave is indispensable for $E_{peak,I}$ to occur and vice-versa: this would initially support our claims that $E_{peak,1}$ corresponds to the electrochemically reversible S—S bond cleaving from $S_2^{2-}{}_{bridging}$ and $S_2^{2-}{}_{terminal}$ given by reactions (1a) and (1b), and $E_{peak,I}$ to the reverse reaction (4a).

2.5.1. AE-MoS_x Electrochemical Conditioning by Oxidative-Reductive and Reductive Cycling: EC, Raman, and XPS Analysis

To further corroborate this, we analyzed the voltammetric profiles of both oxidative-reductive (Figure S13, Supporting Information) and reductive (Figure S14, Supporting Information) cyclic pretreatments along with their respective XPS spectra. For the oxidative-reductive voltammograms, it was observed that $E_{peak,1}$ split into two peaks after continuous cycling irrespective of the electrolyte pH (**Figure 6**a). For AE-MoS_x cycled in a pH 6 electrolyte (Figure 6b), the initially broad precatalytic peak found at $E_{peak,I} \approx -0.68$ V for the first scan decomposed into $E_{peak,III} \approx -0.53$ V and $E_{peak,IV} \approx -0.64$ V. Peak III current density decreased, and peak position shifted positively upon cycling, whereas peak IV emerged as cycling progressed. Plotting of the pH-dependent $E_{peak,III}$ and $E_{peak,IV}$ position in the 0–10 pH range for the 50th oxidative-reductive cathodic scan (Figure 6c) showed that both peaks presented a Nernstian gradient close to −59 mV dec^{-1} ($E_{peak,III} \approx -52 \pm 1$ mV dec^{-1}, $E_{peak,IV} \approx -49 \pm 1$ mV dec^{-1}), consequently leading to an almost constant peak separation. This satisfies the 2 H^+: 2e^- PCET reduction mechanism under which the S—S bond cleaving/dissolution is suggested to occur.

Finally, we compared the relative peak current intensities of $E_{peak,III}$ and $E_{peak,IV}$ to the relative abundance of the S_x^{y-} components found in XPS after electrochemical testing. Amorphous MoS_x materials are deconvoluted with two S $2p_{3/2:1/2}$ spin-orbit doublets (see Figure S7b, Supporting Information): for pristine AE-MoS_x these correspond to a "low binding energy" doublet ascribed to both $S_2^{2-}{}_{terminal}$ and $S^{2-}{}_{unsat}$ with $2p_{3/2}$ and $2p_{1/2}$ binding energies of 161.7 ± 0.1 eV and 162.9 ± 0.1 eV, and a "high binding energy" doublet ascribed to both $S_2^{2-}{}_{bridging}$ and apical S^{2-} ($S^{2-}{}_{apical}$) with $2p_{3/2}$ and $2p_{1/2}$ binding energies of 163.0 ± 0.1 eV and 164.2 ± 0.1 eV.[67,102] An excellent correlation

between relative atomic abundance of the $S_2^{2-}{}_{terminal}/S^{2-}{}_{unsat}$ and $S_2^{2-}{}_{bridging}/S^{2-}{}_{apical}$ components after electrochemical conditioning and the relative $E_{peak,III}/E_{peak,IV}$ current intensity at the 50th scan was found, respectively, in the 0–7 pH range (see Table S2, Supporting Information).

For alkaline pHs, the electrochemical oxidation of the MoS_x film by (4b) along with the thermodynamic instability of its reaction products driven by reaction (5) results in overall thin film dissolution and oxidation of S_x^{y-} components to SO_x^{y-} which prevents any quantitative XPS analysis. This led us to ascribe $E_{peak,III}$ and $E_{peak,IV}$ to the electrochemical cleaving of the S—S bond from $S_2^{2-}{}_{terminal}$ and $S_2^{2-}{}_{bridging}$, respectively. This is in good agreement with the inherent bonding strengths of $S_2^{2-}{}_{terminal}$ and $S_2^{2-}{}_{bridging}$: the Raman vibration of $S_2^{2-}{}_{terminal}$, $\nu(S-S)_{terminal} \approx 516$ cm^{-1}, appears at lower wavenumbers (i.e., softer binding energy) than that of $S_2^{2-}{}_{bridging}$, $\nu(S-S)_{bridging} \approx 555$ cm^{-1}, which indicates that $S_2^{2-}{}_{terminal}$ is more prone to undergo electrochemical cleaving at lower overpotentials than $S_2^{2-}{}_{bridging}$. The excellent correlation between electrochemical and ex situ XPS data supports the use of the latter versus in situ XPS, technically challenging and not available in most research facilities.

The higher content of the "high binding energy" $S_2^{2-}{}_{bridging}/S^{2-}{}_{apical}$ component versus the "low binding energy" $S_2^{2-}{}_{terminal}/S^{2-}{}_{unsat}$ after oxidative-reductive cycling (averaged $S_2^{2-}{}_{terminal}/S^{2-}{}_{unsat}$:$S_2^{2-}{}_{bridging}/S^{2-}{}_{apical}$ ratio of 35:65 vs 46:54 as found in pristine AE-MoS_x) along with the $E_{peak,III}$ current intensity decay upon continuous cycling suggests that S—S cleaving in $S_2^{2-}{}_{terminal}$ proceeds by the cathodic dissolution mechanism (1b) along with electro-oxidative dissolution (4b), the former favored by successive cycling due to the increasingly more positive $E_{peak,III}$ position. For $E_{peak,IV}$, the conversion of $S_2^{2-}{}_{bridging}$ to $S^{2-}{}_{unsat}$ appears to be partially reversible as in both oxidative-reductive and reductive cycling, the $E_{peak,IV}$ current intensity decreases steadily but the peak is still well resolved. In stark contrast, at the reductive cycling voltage region the HER precatalytic feature is almost irreversible: after the first scan, $E_{peak,1}$ current decreases substantially or is almost negligible (see Figures S12b and S14, Supporting Information). Interestingly, the relative $S_2^{2-}{}_{terminal}/S^{2-}{}_{unsat}$:$S_2^{2-}{}_{bridging}/S^{2-}{}_{apical}$ XPS ratio is almost unchanged with respect to pristine AE-MoS_x after reductive cycling across the 0–10 pH range (averaged 49:51 over 0–10 pH results vs initial 46:54, Table S3, Supporting Information). This can be well understood if $S_2^{2-}{}_{bridging}$ and $S_2^{2-}{}_{terminal}$ cleaving selectively undergo mechanisms (1a) and (1b), respectively. The freshly formed $S^{2-}{}_{unsat}$ moieties after $S_2^{2-}{}_{bridging}$ cleaving compensate the loss of $S_2^{2-}{}_{terminal}$ in the XPS S $2p_{3/2:1/2}$ components, keeping their relative ratio balanced.

Investigation of the Raman spectra recorded for samples after having undergone oxidative-reductive and reductive electrochemical conditionings (Figures S15 and S16, Supporting Information) present multiple similarities. The gradual decrease toward higher pH values of both $\nu(S-S)_{terminal}$ and $\nu(S-S)_{bridging}$ Raman modes as compared to $\nu(S_{apical}-Mo)$, which ultimately disappear in neutral to alkaline pHs, corroborates the electrochemical cleaving of $S_2^{2-}{}_{terminal}$ and $S_2^{2-}{}_{bridging}$ moieties at hydrogen precatalytic potentials. It is also observed that both $\nu(Mo-Mo)$ and $\nu(Mo-S)$ vibration bands in the 150–225 cm^{-1} and 285–360 cm^{-1} wavenumber range, respectively, become increasingly unresolved toward higher pH values to ultimately become a broad band: this indicates the loss of the cluster-like structure as found in pristine AE-MoS_x. The lack of any $\nu(Mo-Mo)$ and $\nu(Mo-S)$ band sharpening, contrary to that found for pristine films' electro-oxidation, suggests that morphological restructuring under these electrochemical conditioning protocols is less severe.

Interestingly, the $\nu(S_{apical}-Mo)$ vibrational band seems to split into two additional peaks: one redshifted (≈437 cm^{-1}, sharp and intense) and another one blueshifted (≈483 cm^{-1}), the latter poorly defined toward higher pHs. Tran and co-workers suggested that $S_2^{2-}{}_{terminal}$ dissolution under hydrogen evolving conditions modified the Mo_3 cluster geometry ultimately redshifting the $\nu(S_{apical}-Mo)$ vibration.[71] Indeed, the fact that these bands selectively arise upon reductive cycling within the precatalytic peak $E_{peak,1}$ voltage region informs us that this redox process is indeed directly responsible for the emerging Raman modes. The initial $\nu(S_{apical}-Mo)$ vibration is greatly diminished, but still present at pH 0, which clearly indicates that the band at ≈437 cm^{-1} is a indeed new Raman vibration arising from a weaker $S_{apical}-Mo$ bond. Accordingly, we believe that the band at ≈437 cm^{-1} corresponds to a Mo—S—Mo vibration arising after $S_2^{2-}{}_{bridging}/S^{2-}{}_{apical}$ cleavage, similar to the $\nu(Mo-S-Mo)$ stretching mode found for CE-MoS_x (≈425 cm^{-1}).[103] This would support previous reports which suggested a morphological conversion of AE-MoS_x to CE-MoS_x under HER potentials due to S loss and S—S bond cleavage. In the case of the band at ≈483 cm^{-1}, as already discussed for the pristine electro-oxidation Raman scenario, it is hypothesized to be originated by partially cleaved $S_2^{2-}{}_{terminal}$ moieties: ultimately this band disappears after full dissolution of $S_2^{2-}{}_{terminal}$ moieties.

As for the Mo^{4+}:$Mo^{5+}O_xS_y$: Mo^{6+} XPS relative photoemission ratios, no clear trend can be found neither for the oxidative-reductive nor for the reductive CV conditioning treatments as a function of the pH.

Analysis of Raman and XPS ex situ data for AE-MoS_x samples conditioned by electro-oxidative cycling (see Section S2.5.2 in the Supporting Information for full details) confirms the electrochemical evidence that in acidic pH values the overall MoS_x electro-oxidation is governed by the $S_2^{2-}{}_{terminal}/S^{2-}{}_{unsat}$ electrodissolution (4b) accompanied by a steady Mo^{4+}/Mo^{6+} conversion, whereas in mildly acidic to alkaline pHs the MoS_x electro-oxidation mostly proceeds by the prominent $Mo_xO_y^{z-}$ electro-dissolution.

2.6. AE-MoS_x Activity After Electrochemical Conditioning: Descriptors for Enhanced HER Electrocatalysis

After gathering understanding regarding the implications of the electrochemical cycling pretreatments on the inherent morphology and oxidation state on AE-MoS_x samples, we proceeded to evaluate their impact on the HER electrocatalysis. **Figure 7** shows representative LSVs (*iR* compensated) of AE-MoS_x samples before/after undergoing reductive electrochemically conditioned treatments at pH 0, 3, 6, and 9, respectively. It can be clearly concluded, by comparing the overpotentials required to achieve HER current densities of –2.5 mA cm^{-2} (η_{HER}@ |2.5 mA cm^{-2}| = $\eta_{initial} - \eta_{final}$), a figure of merit attainable at the HER overpotential window monitored for all

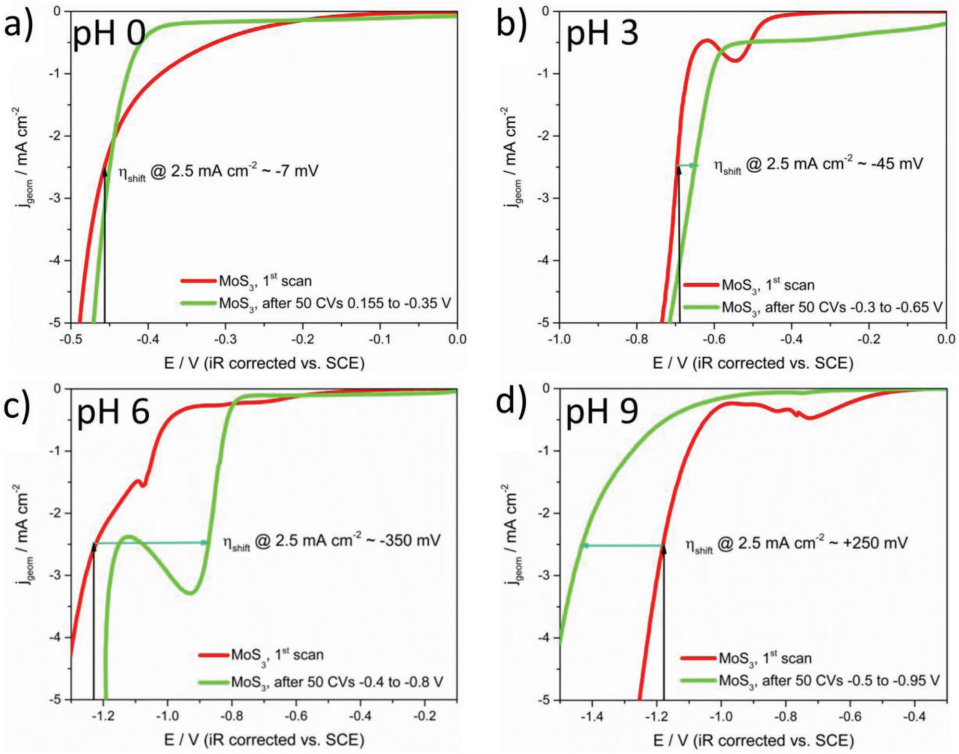

Figure 7. Representative voltammograms obtained for AE-MoS_x films before (red) and after (green) undergoing reductive electrochemical conditioning at in a) pH 0 (0.5 M H_2SO_4), b) pH = 3 (82/18 v/v mixture of 0.1 M citric acid/0.1 M sodium citrate), c) pH = 6 (11.5/88.5 v/v mixture of 0.1 M citric acid/0.1 M sodium citrate), and d) pH = 9 (14.4/85.6 v/v mixture of 0.1 M HCl/0.05 M sodium tetraborate). Scan rate: 50 mV s^{-1}.

pH values in this study, that the electrochemical conditioning treatments performed do have an effect on the HER electrocatalysis. Samples conditioned at very acidic pHs (pH 0) present the faintest modification in their performance; at mildly acidic conditions (pH 3) their overall effect is negative, whilst in quasi-neutral conditions (pH 6) there is a substantial enhancement in the HER electrocatalysis. Finally, for alkaline conditions (pH 9), the electrochemical conditionings studied are again detrimental for the HER electrocatalysis. In an attempt to correlate any modification in HER electrocatalysis with physical properties of the AE-MoS_x samples, we plotted η_{HER}@ |2.5 mA cm^{-2}| as a function of the most commonly used HER descriptors in the amorphous MoS_x literature across the studied pH range according to their XPS relative abundance: "high binding energy" $S_2^{2-}{}_{bridging}/S^{2-}{}_{apical}$, Mo^{4+}, S^{2-}/S_2^{2-}:Mo^{4+} ratio (only including unoxidized Mo and S surface species), and total S:Mo ratio (accounting for oxidized Mo and S surface species).

For samples undergoing the "electro-oxidation" cycling (**Figure 8**), there is a clear correlation between the HER electrocatalysis and the relative surface content of $S_2^{2-}{}_{bridging}/S^{2-}{}_{apical}$ and Mo^{4+} species. Surprisingly, the samples which presented enhanced HER electrocatalysis were the ones which presented lower Mo^{4+} and $S_2^{2-}{}_{bridging}/S^{2-}{}_{apical}$ species contents, and vice versa. This contradicts previous reports which correlated higher hydrogen turnover frequencies with incremental $S_2^{2-}{}_{bridging}/S^{2-}{}_{apical}$ species and Mo^{4+} contents.[78] This leads us to believe that partially oxidized, undercoordinated Mo moieties generated during electro-oxidation present promoted HER activities compared to the untreated AE-MoS_x cluster-like structure, somehow involving the generation of more active $S_2^{2-}{}_{terminal}/S^{2-}{}_{unsat}$ moieties.

For samples treated by the "oxidation-reduction" cycling (Figure S18, Supporting Information), no clear trend can be found for the $S_2^{2-}{}_{bridging}/S^{2-}{}_{apical}$ and Mo^{4+} species relative surface content, but it seems to be present in the S^{2-}/S_2^{2-} : Mo^{4+} ratio instead: higher sulfide contents lead to improved HER activity and vice versa. The well-established proton-accepting role of sulfur sites in MoS_2 electrocatalysis supports this experimental trend.[13,104] Finally, the AE-MoS_x samples electrochemically conditioned by "reductive" cycling (**Figure 9**) present HER electrocatalytic properties correlating with "high binding energy" $S_2^{2-}{}_{bridging}/S^{2-}{}_{apical}$ and S^{2-}/S_2^{2-} : Mo^{4+} ratio (the latter to a minor extent): higher sulfide contents and lower $S_2^{2-}{}_{bridging}/S^{2-}{}_{apical}$ promoted HER on AE-MoS_x. This trend is very valuable as it informs that not only sulfur is the main HER active site triggered under selective cathodic preconditioning, but also that the simultaneously electrochemically induced $S_2^{2-}{}_{bridging}$ cleaving and $S_2^{2-}{}_{terminal}$ dissolution leads to unsaturated $S^{2-}{}_{unsat}$ moieties which are ultimately the proton-accepting sites.

It is also noteworthy to compare the maximum positive/negative electrocatalytic effects obtained as a function of the electrochemical preconditioning employed, giving an order as follows: reductive (from −350 to +250 mV) > electro-oxidative (from −290 to + 210 mV) > oxidative-reductive (from −220 to + 150 mV). Hence, selective electrochemical cycling within the precatalytic HER and electro-oxidative windows, trigger electrochemically driven AE-MoS_x surface restructuring that

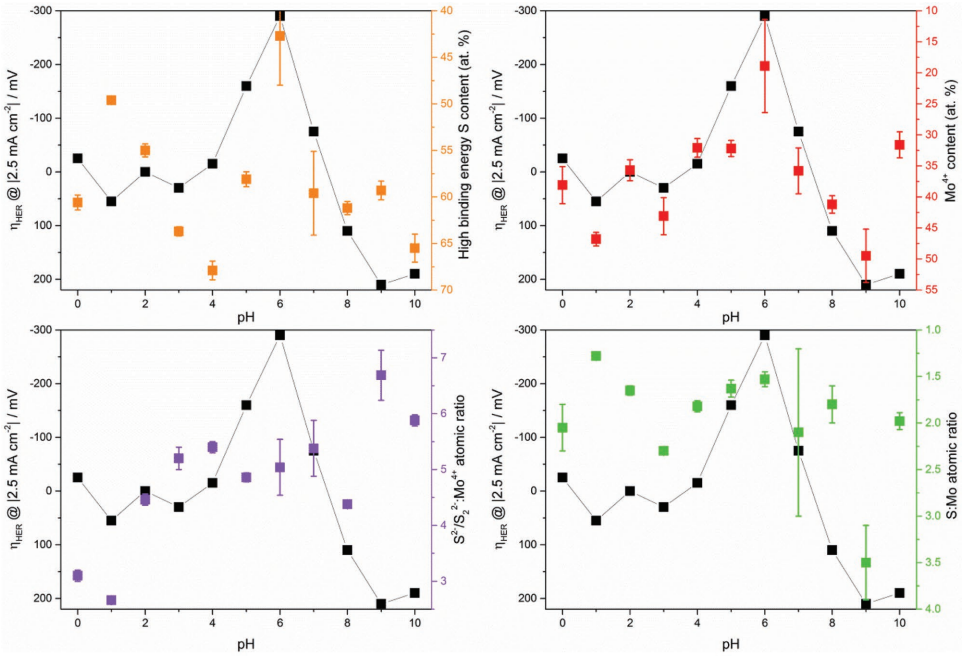

Figure 8. Summary of η_{HER}@ |2.5 mA cm^{-2}| as a function several AE-MoS_x descriptors across the 0–10 pH range after electro-oxidative AE-MoS_x conditioning: a) "high binding energy" $S_2^{2-}{}_{bridging}/S^{2-}{}_{apical}$ content, b) Mo^{4+} content, c) S^{2-}/S_2^{2-}:Mo^{4+} ratio, and d) total S:Mo ratio. At% units correspond to relative XPS percentages within the Mo 3d and S 2p deconvoluted components.

govern the HER performance, namely, $S_2^{2-}{}_{bridging}$ cleaving and $S_2^{2-}{}_{terminal}$ dissolution, and partially oxidized undercoordinated Mo moieties generation, respectively. Analogous enhancements on crystalline MoS_2 were found upon reductive electrochemical treatments, initially allocated to lower chalcogen-to-metal ratios exposing more Mo-edge sites[100] and later ascribed to the basal plane activation by formation of S vacancies below −1 V versus RHE.[42] For oxidative-reductive conditioning, the partial electrochemical reversibility of the aforementioned phenomena limits their impact on the HER electrocatalysis, as their generation

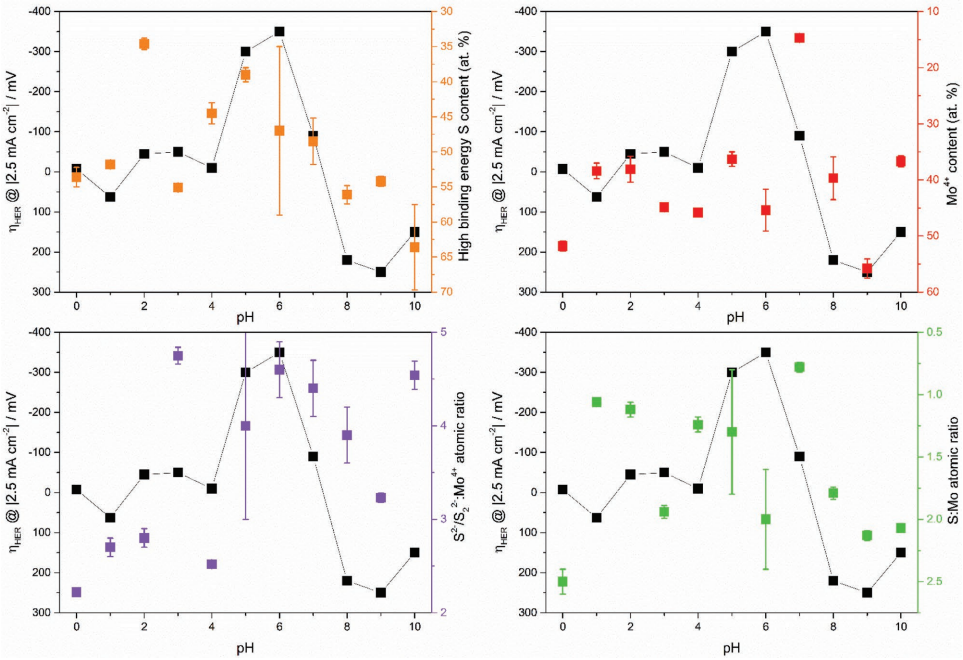

Figure 9. Summary of η_{HER}@ |2.5 mA cm^{-2}| as a function several AE-MoS_x descriptors across the 0–10 pH range after reductive AE-MoS_x conditioning: a) "high binding energy" $S_2^{2-}{}_{bridging}/S^{2-}{}_{apical}$ content, b) Mo^{4+} content, c) S^{2-}/S_2^{2-}: Mo^{4+} ratio, and d) total S:Mo ratio. At% units correspond to relative XPS percentages within the Mo 3d and S 2p deconvoluted components.

at anodic/cathodic regions will be inevitably followed by their partial depletion/reinstatement at the opposite voltage range.

In addition to this, specific pH ranges can be identified where the AE-MoS_x surface is either insensitive or dramatically affected by the electrochemical conditioning methods employed. Samples preconditioned at pH 4 present the lowest overpotential modifications (reductive: −10 mV, electro-oxidative: −15 mV, oxidative-reductive: +30 mV), whereas those conditioned at pH 6 (reductive: −350 mV, electro-oxidative: −290 mV, oxidative-reductive: −220 mV) and pH 9 (reductive: +250 mV, electro-oxidative: +210 mV, oxidative-reductive: +150 mV) present the most positive and negative impact on HER electrocatalysis, respectively. These provide insight on specific pH regions under which AE-MoS_x activity and/or stability may be exploited for long-term operating conditions.

Thus, we can conclude that monitoring of specific HER descriptors across the whole pH spectrum, specifically those related to sulfide moieties ($S_2^{2-}{}_{bridging}/S^{2-}{}_{apical}$ and S^{2-}/S_2^{2-}:Mo^{4+} ratio), allow the correlation of the experimental hydrogen electrocatalysis observed with surface-dependent AE-MoS_x properties.

2.7. AE-MoS_x Long-Term HER Performance: Stability and Accelerated Durability Testing

Assessment of the stability and durability of HER catalysts is paramount for their implementation in commercial PEM electrolyzer stacks. However, recent reports have highlighted that no standardized stability test protocol has been adopted in the HER field to evaluate electrocatalytic lifetimes.[105,106] For oxygen evolution electrocatalysts, however, several benchmarking tests have been proposed, most of them comprising chronopotentiometric measurements to monitor catalyst stability (with durations not less than 2 h)[107] and continuous potential cycling at high voltage scan rates. The latter have proven to give representative information on electrocatalyst durability at shorter timescales, comparable to that obtained at PEM electrolyzer average lifetimes (50 000 h).[108] Here we opted to evaluate pristine AE-MoS_x hydrogen evolution stability and durability across the 0–10 pH range by recording, under 1500 rpm stirring, chronopotentiograms of 12 h duration at a constant cathodic current density of −10 mA cm^{-2} (HER benchmarking current density),[109] and by acquiring 3000 cyclic voltammograms at 100 mV s^{-1} scan rate with a cathodic voltage limit set to attain a maximum current density of −10 mA cm^{-2}.

A compilation of the 12 h stability test results is shown in **Figure 10**a,b. At very acidic environments ($0 \leq pH \leq 2$) a significant upward increase in both initial ($t = 0 \pm 10$ min) and final ($t = 12$ h $\pm$ 10 min) HER overpotentials was found toward higher pH values. It is widely established that transition metal sulfides dissolve in acidic media under HER operating conditions due to sulfur atoms loss.[110,111] This property is key in AE-MoS_x, as the electrochemically induced $S_2^{2-}{}_{bridging}$ cleaving and $S_2^{2-}{}_{terminal}$ dissolution at cathodic potentials, despite of

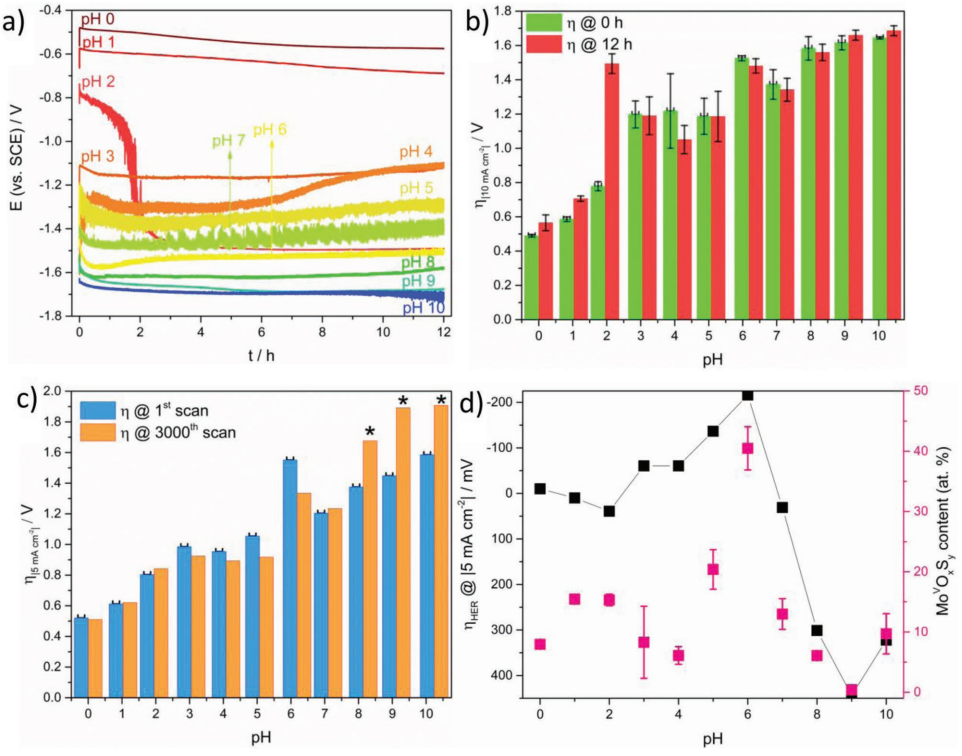

Figure 10. a) Representative chronopotentiograms recorded during AE-MoS_x HER stability measurements (12 h galvanostatic electrolysis at j_{geom} = −10 mA cm^{-2}). b) Averaged (±10 min) initial (green) and final (red) overpotentials to sustain j_{geom} = −10 mA cm^{-2} for 12 h. c) Initial (blue) and final (orange) HER η_{HER}@ |5 mA cm^{-2}| obtained during accelerated durability testing on AE-MoS_x (3000 CVs, 100 mV s^{-1}). Values with * indicate approximate overpotentials due to experimental currents not achieving −5 mA cm^{-2} at the evaluated voltage window. d) Summary of η_{HER}@ |5 mA cm^{-2}| as a function $Mo^{5+}O_xS_y$ relative XPS content across the 0–10 pH range after accelerated durability testing.

the inevitable sulfur loss, are responsible for the generation of the S^{2-}_{unsat} HER active sites. At pH 2, we suspect that the high AE-MoS_x instability, along with the dissolution of the Au electrode layer promoted by the high chloride concentration in the buffered electrolyte (found after physical inspection of the samples' surfaces), explain the dramatic HER overpotential increase. Surprisingly, in mildly acidic conditions ($3 \leq pH \leq 6$) the AE-MoS_x samples present almost unchanged HER performances, slightly improved at pH 4 values (≈167 mV lower average overpotential) and to a lesser extent at pH 6 (≈45 mV lower average overpotential). Finally, for neutral-to-alkaline environments ($7 \leq pH \leq 10$), the HER continuous performance seems almost constant in neutral pHs (7–8) whereas it clearly worsens in alkaline pHs (9–10), with starting overpotentials increasingly higher toward higher pHs. As mentioned previously, the increasingly higher inherent thermodynamic instability of AE-MoS_x toward alkaline environments supports the worsened HER performance observed.

Upon analysis of the overall initial HER overpotential trends, it is of particular relevance that both the $3 \leq pH \leq 5$ and pH 7 regions break the generally upward trend: these might represent pH environments of AE-MoS_x improved electrochemical activity and stability.

A compilation of the accelerated durability cycling testing for η_{HER}@ $|5\ mA\ cm^{-2}|$ across the 0–10 pH range is shown in Figure 10c (for representative cycling voltammograms, see Figure S19, Supporting Information). The experimental trends are in good agreement those obtained for chronopotentiometry experiments: acidic ($0 \leq pH \leq 2$) and neutral-to-alkaline ($7 \leq pH \leq 10$) pH environments present increased HER overpotentials after voltammetric cycling, significantly higher in the alkaline scenario. However, AE-MoS_x tested in mildly pH conditions ($3 \leq pH \leq 6$), contrary to chronopotentiometry experiments, present enhanced HER electrocatalytic activities. This supports previous experimental evidence that, under these pH conditions, AE-MoS_x HER electrocatalysis does not only seem more favorable (maximized HER activities after electrochemical conditioning for pH 6) but can also be sustained under short duty and accelerated durability testing conditions.

Ex situ Raman (**Figure 11**) and XPS spectroscopy measurements after accelerated durability tests provide insight on their origin. Compared to pristine AE-MoS_x, both ν(Mo—Mo) and ν(Mo—S) vibration bands in the 150–225 and 285–360 cm^{-1} wavenumber range, respectively, become increasingly unresolved toward higher pH values leading to their complete disappearance in favor of a broad band from pH 4 upward. Hence, the previously well-defined AE-MoS_x cluster-based structure is irreversibly modified after accelerated HER operation conditions. Analogously, the $\nu(S_{apical}—Mo)$, $\nu(S—S)_{terminal}$, and $\nu(S—S)_{bridging}$ vibrations found at 447, 516, and 555 cm^{-1} in pristine thin films, respectively, undergo substantial modifications.

As previously reported for AE-MoS_x undergoing reductive electrochemical preconditioning, in acidic environments ($0 \leq pH \leq 3$), the signal intensities of $\nu(S—S)_{terminal}$ and $\nu(S—S)_{bridging}$ gradually decreased at increasing pH values, the former completely disappearing at pH 1 and the latter blueshifting and ultimately only observed as a shoulder up to pH 3. Analogously, the $\nu(S_{apical}\text{-}Mo)$ vibrational band splits into two additional peaks: one redshifted (≈437 cm^{-1}, ascribed to Mo—S—Mo vibration similar to those found for CE-MoS_x) and another one blueshifted (≈483 cm^{-1}, ascribed to partially cleaved $S_2^{2-}{}_{terminal}$ moieties), the latter poorly defined toward upward pHs. From mildly acidic to neutral pHs ($4 \leq pH \leq 7$), the Mo=O (≈880 cm^{-1}) and $Mo(=O)_2$ (≈960 cm^{-1}) vibrations steadily surfacing in acidic pHs govern the Raman spectra, leaving the unresolved (Mo—Mo) and (Mo—S) bands in the 100–600 cm^{-1} overlapped as a shoulder. Finally, the thermodynamic instability of surface molybdenum oxides in alkaline environments implies the dissolution of Mo_xO_y species responsible for Mo=O and $Mo(=O)_2$ vibrations, which ultimately justifies the resurfacing of (Mo—Mo) and (Mo—S) bands from nondissolved MoS_x.

Component analysis of ex situ XPS spectra on the freshly tested samples shows no clear trend involving the previously employed HER descriptors (see Figure S20,

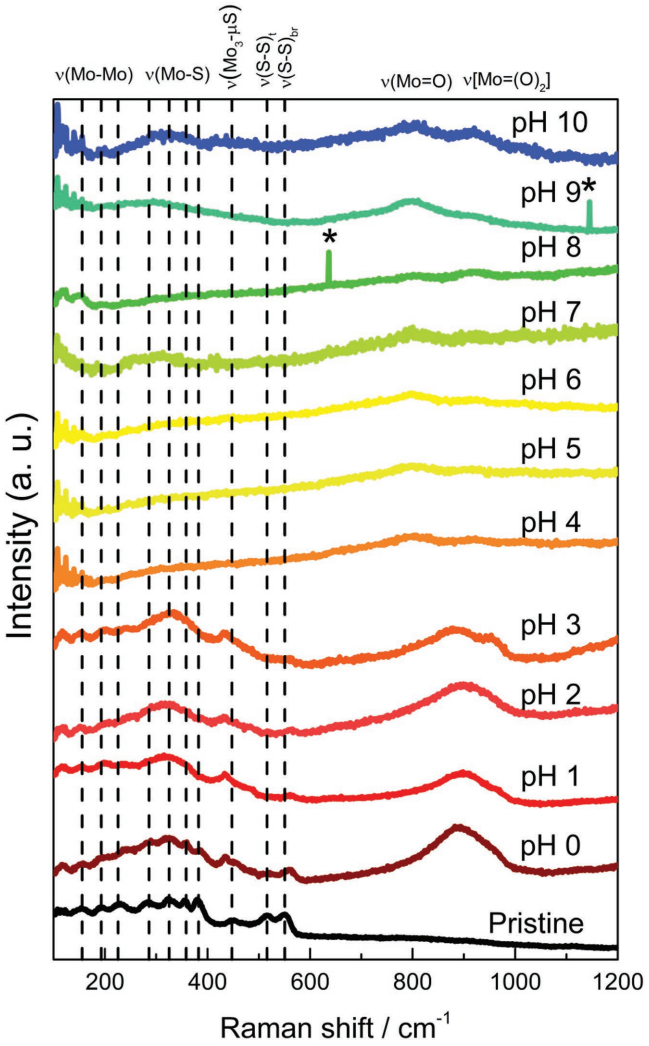

Figure 11. Stacked Raman spectra (532 nm laser excitation, 100–1200 cm^{-1} range) of pristine (black), and AE-MoS_x thin films after accelerated durability testing (3000 CVs, 100 mV s^{-1}) across the 0–10 pH range. Dashed vertical lines refer to characteristic AE-MoS_x vibration modes. Raman features marked with an asterisk originated from a cosmic ray.

Supporting Information). However, when plotting the oxygen-incorporated $Mo^{5+}O_xS_y$ relative surface content along with the η_{HER}@ |5 mA cm^{-2}| across the 0–10 pH range (Figure 10d), a clear positive correlation between enhanced HER performances and $Mo^{5+}O_xS_y$ contents was found: at pH 6, where the $Mo^{5+}O_xS_y$ relative surface content is found to be the highest (≈40.5± 3.6 at%), the biggest HER overpotential shift is also achieved (≈−220 mV). As stated in Section 2.2, the presence of $E_{peak,2}$ and $E_{peak,3}$ at pH ≥ 5 supported the instability of $Mo^{5+}O_xS_y$ in acidic environments, which is in good agreement with the results obtained in both Raman (faint Mo=O and $Mo(=O)_2$ vibration intensities) and XPS measurements ($Mo^{5+}O_xS_y$ contents lower after electrochemical testing than as-prepared AE-MoS_x: < 18.6± 0.2 at%) for samples tested in acidic electrolytes. Remarkably, at pH values higher than 4 (i.e., when the HER electrocatalysis is greatly enhanced), the intense Mo=O and $Mo(=O)_2$ vibrations allocated to molybdenum oxide species as well as the sharp increase in oxygen-containing $Mo^{5+}O_xS_y$ surface species indicate a convergence between oxygen incorporation in the AE-MoS_x film and enhanced HER electrocatalysis.

Thus, this leads us to the conclusion that the most active HER AE-MoS_x phase involves, under hydrogen evolving conditions, the formation of oxygen-incorporated (i.e., sulfur deficient) $Mo^{5+}O_xS_y$ species. As the undeniable role of $S_2^{2-}{}_{bridging}$ and $S_2^{2-}{}_{terminal}$ in the HER catalysis has been proven in this study, their selective electrochemical cleaving lead, respectively, to unsaturated sulfur (reaction 1a) and molybdenum (reaction 1b) sites. We hypothesize, accordingly, that both phenomena synergistically assist in the generation of the HER active sites. Indeed, a very recent report has correlated enhanced hydrogen electrocatalysis in amorphous MoS_x materials at neutral pH values with an internal reorganization of a bridging $S_2^{2-}{}_{bridging}$ ligand to an $S_2^{2-}{}_{terminal}$ configuration by in situ Raman measurements.[72] This reorganization in the Mo_3-thio cluster-like structure was proposed to yield undercoordinated Mo−Mo sites which synergistically promoted the HER. However, the $S_2^{2-}{}_{terminal}$ dissolution found in this study supported by electrochemical, Raman, and XPS experiments leads us to believe that the bridging $S_2^{2-}{}_{bridging}$ ligand adopts an $S^{2-}{}_{unsat}$ configuration instead.

The AE-MoS_x electrocatalysis under hydrogen evolution conditions is then proposed to operate as follows. In acidic pH values (0 ≤ pH < 4), the predominant HER active sites are those comprising $S^{2-}{}_{unsat}$ formed after $S_2^{2-}{}_{bridging}$ cleaving as unsaturated Mo sites (although more active to the HER) will be prone to oxy(hydro)xide formation by hydration and subsequently present thermodynamic instability. On the other hand, in mildly acidic to neutral pHs (4 ≤ pH < 7), the unsaturated Mo^{5+} as found in $Mo^{5+}O_xS_y$ species will no longer dissolve in the electrolyte, compensating for the $S^{2-}{}_{unsat}$ loss and opening an alternative HER route similar to that proposed by Tran et al.[71] At this stage we must also take into account the variations of the inherent HER kinetics across the studied pH range to understand their interplay with the proposed active sites. At 0 ≤ pH ≤ 2, where the AE-MoS_x HER mechanism is expected to undergo by H_3O^+ electroreduction, we believe that the cleaved $S_2^{2-}{}_{bridging}$ moieties (which act as proton-accepting sites, as suggested by in operando Raman studies) are the HER active sites. At higher pH values, as HER electrocatalysis should operate by the water reduction/splitting mechanism, we believe that the freshly cleaved $S^{2-}{}_{unsat}$ from $S_2^{2-}{}_{bridging}$ moieties are less electrocatalytically active, and only when $Mo^{5+}O_xS_y$ species are thermodynamically stable at the surface (pH > 4) the HER can be successfully catalyzed. As previous in operando studies suggest an absence of v(Mo−H) at hydrogen evolving potentials, we believe that the HER mechanism on $Mo^{5+}O_xS_y$ species necessarily involves the protonation of the Mo=O moieties through O−H bond cleavage and sequential electron transfer. Finally, at neutral to alkaline pHs (7 ≤ pH ≤ 10), the instability of both $S^{2-}{}_{unsat}$ and $Mo^{5+}O_xS_y$ leads to the prominent formation of solution soluble molybdenum oxides with worsened HER kinetics.

3. Conclusion

This study has explored the impact of electrolyte pH on the inherent and HER electrochemistry of electrodeposited AE-MoS_x films and its implications in long term operation conditions. Analysis of the precatalytic HER features along with EC and XPS using buffered electrolytes have corroborated the simultaneous cleaving of $S_2^{2-}{}_{bridging}$ and $S_2^{2-}{}_{terminal}$ dissolution along with a proposed reduction of $Mo^{5+}O_xS_y$ species to MoO_2 only observed in the 5 ≤ pH ≤ 10 range.

The previously reported distinctive EC-dependent electro-oxidation features have been rationalized using PCET theory, demonstrating a modification in the complex electro-oxidation mechanism. Pristine AE-MoS_x satisfies a 1 H^+: 2e^- PCET across the studied pH range ascribed to the oxidation of the Mo^{4+} moieties to Mo^{6+} analogous to crystalline MoS_2, whereas HER preconditioned AE-MoS_x presents two distinct electro-oxidation behaviors. In acidic electrolyte this cannot be unambiguously understood: XPS and Raman investigations suggest a mechanism comprising overall $S_2^{2-}{}_{terminal}/S^{2-}{}_{unsat}$ electro-dissolution accompanied by a gradual Mo^{4+}/Mo^{6+} conversion to generate MoO_x species. In the 7 ≤ pH ≤ 10 range, it seems to operate by a sequential 1 H^+: 1e^- PCET arising from partial reinstatement of previously cleaved $S_2^{2-}{}_{bridging}$ ligands and $S_2^{2-}{}_{terminal}$ ligands dissolution, followed by a 2 H^+: 1e^- PCET corresponding to the oxidation of MoO_2 to MoO_4^{2-}.

Electrochemical conditioning by cycling within reductive/electro-oxidative/oxidative-reductive voltage results in pronounced changes in the HER performance giving an order of |η_{HER}|@ |2.5 mA cm^{-2}| enhanced/detrimental electrocatalytic effects as follows: reductive (from −350 to +250 mV) > electro-oxidative (from −290 to + 210 mV) > oxidative-reductive (from −220 to + 150 mV). The pH ranges responsible for the most enhanced and detrimental performances are 4 ≤ pH ≤ 6 and 8 ≤ pH ≤ 10, respectively. The triggered surface modifications mainly consisted of $S_2^{2-}{}_{bridging}$ cleaving and $S_2^{2-}{}_{terminal}$ dissolution (reduction) and partially oxidized undercoordinated Mo sites generation with predominance of $S_2^{2-}{}_{terminal}/S^{2-}{}_{unsat}$ moieties (electro-oxidative). Raman spectra analysis corroborated the reductive $S_2^{2-}{}_{bridging}$ cleaving and $S_2^{2-}{}_{terminal}$ dissolution (suppressed vibration modes under reductive potentials), identifying additional bands here ascribed to partially cleaved S moieties.

Finally, 12 h constant current hold and accelerated cyclic voltammetry experiments revealed that AE-MoS_x films, contrary

to conventional testing conditions reported in literature, retain their initial activity and provide more stable performances in the $3 \leq pH \leq 5$ range. Combined analysis of XPS and Raman measurements suggest the oxygen-containing, S-deficient $Mo^{5+}O_xS_y$ surface species as the responsible sites for the HER catalysis in this range. Although cleaved $S_2^{2-}{}_{bridging}$ ligands generating $S^{2-}{}_{unsat}$ proton-accepting sites explain the HER activity of AE-MoS_x in acidic electrolytes, the thermodynamic stability of $Mo^{5+}O_xS_y$ species along with the water reduction HER mechanism satisfied in mildly acidic to alkaline electrolytes explain the key role of $Mo^{5+}O_xS_y$. The pivotal knowledge gathered from our pH-dependent benchmarking experiments, we believe, will enable to accelerate the deployment TMD-based electrolyzers and shed light into understanding the interplay between surface properties and electroactivity maximization for other earth-abundant HER materials.

4. Experimental Section

Electrochemical Measurements: Electrochemical measurements on electrodeposited MoS_x thin films were made in a three-electrode configuration using a PC-controlled PGSTAT128N potentiostat (Metrohm Autolab B.V., Netherlands) with a thermostated cell (295 ± 2K). MoS_x thin film-modified Si (1 mm)/Si thermal oxidation layer (1 µm)/Ti (10 nm)/Au (100 nm) substrates prepared by sputtering deposition and mechanical dicing (5 × 15 mm, IMB-CNM, Universitat Autònoma de Barcelona, Spain) were used as working electrodes. A saturated calomel electrode (SCE, BAS Inc., Japan) and a bright Pt mesh (Alfa Aesar, U.K.) were used as reference and counter electrodes, respectively. To prevent possible platinum contamination onto the pristine MoS_x thin films, the Pt counter electrode was encapsulated in a glass tube with a fritted junction.

Electrolytes employed for pH-controlled inherent electrochemistry and HER measurements were prepared as follows. For pH≈0, a 0.5 M H_2SO_4 (95% v/v, Fisher Scientific) acid solution was employed. pH 1–2 solutions were obtained by mixing aliquots of 0.2 M HCl (37% v/v ACS, Sigma-Aldrich) and 0.2 M KCl (anhydrous, ACS ≥ 99%, Sigma-Aldrich) electrolytes. pH 3–6 buffered electrolytes were obtained by mixing varying volumes of 0.1 M citric acid monohydrate (ACS ≥ 99%, Sigma-Aldrich) and 0.1 M sodium citrate dihydrate (≥99% FG, Sigma-Aldrich) solutions. The phosphate buffered saline (PBS) pH 7 electrolyte was prepared by mixing 6.15 mL of a 1 M potassium phosphate dibasic trihydrate (≥99%, for molecular biology, Sigma-Aldrich), and 3.85 mL of a 1 M potassium phosphate monobasic (≥99%, for cell culture, Sigma-Aldrich). Finally, pH 8–10 buffered electrolytes were prepared by mixing 0.05 M sodium tetraborate (anhydrous, BioUltra ≥ 99%, Sigma-Aldrich) with 0.1 M HCl (for pH 8–9) or 0.1 M NaOH (ACS ≥ 97%, pellets, Sigma-Aldrich) (for pH 10). All electrolytes were brought to volume in 100 mL volumetric flasks with ultrapure water (Millipore Mili-Q Direct 8, resistivity not less than 18.2 MΩ cm), testing their final pH using a 3-point calibrated Mettler-Toledo FiveEasy FE20 pH bench meter coupled to a Mettler-Toledo LE438 pH electrode (Greifensee, Switzerland). Oxygen-free conditions during electrochemical experimentation were achieved after purging the EC cell with N_2 (Oxygen-free grade, BOC Gases plc), and maintained by applying a positive N_2 atmosphere above the electrolyte surface. All electrochemical glassware was cleaned overnight by use of a dilute solution of $KMnO_4$ (ACS ≥ 99%, Sigma-Aldrich) in concentrated H_2SO_4 (>95% analytical grade, Fisher Scientific) followed by thorough rinsing with ultrapure water.

pH-dependent inherent electrochemical activity of as-prepared electrodeposited MoS_x thin films was evaluated by acquiring one cyclic voltammogram from 0.7 to −1.2 V versus SCE. For MoS_x activation pretreatment studies, a 50 cyclic voltammogram protocol was employed, where both anodic and cathodic limits were modified based on the inherent electrochemical features observed in the voltammogram of the as-prepared sample. Three main pretreatments were investigated: electro-oxidative (lower voltage selected close to OCP values, upper voltage selected past the electro-oxidation features), oxidative-reductive (lower voltage selected past the first cathodic prewave peak, upper voltage selected past the electro-oxidation features) and reductive (lower voltage selected past the first cathodic prewave peak, upper voltage selected close to OCP values). Linear sweep voltammograms ($E_{anodic} = E_{SCE} + E_{H^+/H_2} - 0.059pH$, to $E_{cathodic} = -1.2\ V - 0.059pH$) and electrochemical impedance spectroscopy measurements (voltage range: −0.1 to −1.4 V vs SCE, 200 mV steps, frequency range: 10^{-1}–10^5 Hz, voltage amplitude = 10 mV) were recorded before and after the activation pretreatment step to account for modifications in both HER activities and *iR* compensation corrections.

For long-term potentiodynamic durability testing, an initial linear sweep voltammogram was recorded from 0.7 to −1.2 V versus SCE on as-prepared MoS_x thin films under 1500 rpm exerted by a magnetic stirring bar controlled by a stirring plate to establish the anodic and cathodic limits. The upper voltage limit was selected close to OCP values, whereas the cathodic limit was selected to achieve HER geometric current densities of −10 mA cm^{-2}. Under these conditions, 3000 cyclic voltammograms were recorded at 1500 rpm and positive N_2 pressure for all the electrolytes tested at a voltage scan rate of 100 mV s^{-1}. For stability measurements, a 12 h chronopotentiometry experiment was set to monitor the overpotential required to sustain a constant HER geometric current density of −10 mA cm^{-2}, with experimental conditions equivalent to those used for potentiodynamic experiments (1500 rpm, positive N_2 pressure).

All electrochemical experiments were repeated no less than three times to ensure reproducibility.

Preparation of Amorphous MoS_x Thin Films: Amorphous MoS_x thin films were deposited onto Si/Ti (10 nm)/Au (100 nm) substrates by electrochemical deposition from a freshly prepared, deaerated electrolyte solution containing 2×10^{-3} M $(NH_4)_2[MoS_4]$ (99.97% trace metal analysis, Sigma-Aldrich) and 0.1 M $NaClO_4$ (ACS ≥ 98%, Sigma-Aldrich). In this setup, a double-junction saturated Ag/AgCl reference electrode (Sigma-Aldrich) and a bright Pt mesh counter electrode (Alfa Aesar, UK) were employed. Analogously to HER experiments, the Pt counter electrode was encapsulated in a glass vial with a fritted junction to prevent Pt redeposition onto the deposited MoS_x thin films. A deposition area on Si/Ti/Au chips ($5 \times 5\ mm^2$) was selectively exposed to the electrolyte by insulating the remaining working electrode surface with hydrophobic PTFE tape. Electrodeposition was carried out with neither rotation nor N_2 bubbling to prevent alterations in the deposition rate from the effects of convection. Preliminary deposition rate studies were performed by depositing MoS_x thin films at various charge densities. Anodic electrodeposition (AE) was performed at a constant voltage of +0.1 V versus Ag/AgCl, while cathodic electrodeposition (CE) was performed at −1 V versus Ag/AgCl. MoS_x thin film thickness versus charge density plots (Figure S3, Supporting Information) were obtained after three independent height profile measurements of each MoS_x-modified sample using a Dektak 3ST surface Profilometer (Veeco, USA). For inherent electrochemistry and HER experiments on AE-MoS_x, an approx. thickness of 100 nm (33.7 mC cm^{-2}) was employed in all samples, assuming a 100% Faradaic deposition efficiency.

Physical Characterization of Amorphous MoS_x Thin Films: X-ray photoelectron spectroscopy (XPS) measurements were performed in a Thermo Scientific K-Alpha system (Thermo Scientific, UK) as well as in a Kratos AXIS ULTRA system (Kratos, UK): both used a microfocused monochromatic aluminum X-ray source (Al Kα, 1486.6 eV, 12 kV), a charge neutralizer filament to prevent surface charging, and working pressures below 5×10^{-9} mbar. Three independent and nonoverlapping XPS analysis positions were acquired, using spot sizes of 400 × 800 µm (Thermo Scientific) and 0.5 mm^2 (Kratos), on each MoS_x sample mounted on a clean stainless steel plate. For low resolution survey spectra, 150 eV (Thermo Scientific)/80 eV (Kratos) pass energies and 0.4 eV (Thermo Scientific)/0.5 eV (Kratos) step sizes were employed (dwell time: 10 ms), whereas for high-resolution spectra pass energies

and step sizes of 40 eV (Thermo Scientific)/20 eV (Kratos) and 0.1 eV were selected (dwell time: 100 ms). All high-resolution spectra were energy-corrected to the adventitious C 1s peak set to 284.6 eV, and processed using the CASA XPS software (version 2.3.18PR1.0). For peak-deconvolution, Shirley backgrounds and Gaussian-Lorentzian (30) lineshapes were selected. Mo 3d spectra were fitted by applying a 3:2 area ratio constraint and 3.1 eV separation on the $3d_{5/2:3/2}$ spin-orbit doublets, whereas S 2p spectra were fitted by applying a 2:1 area ratio constraint and 1.2 eV separation on the $2p_{3/2:1/2}$ spin-orbit doublets.[103,112,113]

Raman spectroscopy measurements were conducted on a Renishaw inVia Raman microscope (Renishaw, UK) using a 532 nm laser and an interchangeable 50 cm^{-1} low pass filter (Renishaw, UK) previously calibrated by the 520 cm^{-1} peak found in a Si wafer standard. Low resolution survey spectra were recorded in the 100–2500 and 100–1200 cm^{-1} wavelength ranges by three cumulative acquisitions of 10 s. For high-resolution Raman spectra at the characteristic MoS_x vibrational frequencies (100–800 cm^{-1}), three cumulative acquisitions of 30 s were employed. In all cases, two nonoverlapping regions were investigated per MoS_x thin film sample, using a 20x objective lens and 10% laser power. Higher magnification lenses at the selected laser power and exposure times lead to lased-induced MoS_x crystallization as reported by Nguyen et al.[99]

Supporting Information

Supporting Information is available from the Wiley Online Library or from the author.

Acknowledgements

The authors thank the EPSRC for support through funding for the Centre for Doctoral Training in Fuel Cells and their Fuels (D.E.L., N.V.R., EP/G037116/1 and EP/L015749/1). The authors would also like to thank Dr. Francisco Javier del Campo and Dr. Joaquima López García at the IMB-CNM (CSIC) for the preparation of the Si/Ti/Au electrodes used in this work, and Dr. Jacqueline K. Deans at the Centre for Chemical and Materials Analysis (School of Chemistry, University of Birmingham) for support during Raman spectroscopy measurements. X-ray photoelectron spectra were obtained at the National EPSRC XPS Users' Service (NEXUS) at Newcastle University, and EPSRC Mid-Range Facility, and at the Nanoscale and Microscale Research Centre (NMRC) at the University of Nottingham by Dr. Emily Smith.

Conflict of Interest

The authors declare no conflict of interest.

Keywords

active sites, benchmarking, hydrogen evolution, molybdenum sulfide, pH

Received: August 21, 2018
Revised: October 10, 2018
Published online: January 4, 2019

[1] A. Tatin, J. Bonin, M. Robert, *ACS Energy Lett.* **2016**, *1*, 1062.
[2] S. Chu, Y. Cui, N. Liu, *Nat. Mater.* **2017**, *16*, 16.
[3] J. A. Turner, *Science* **2004**, *305*, 972.
[4] S. Ardo, D. Fernandez Rivas, M. A. Modestino, V. Schulze Greiving, F. F. Abdi, E. Alarcon Llado, V. Artero, K. Ayers, C. Battaglia, J.-P. Becker, D. Bederak, A. Berger, F. Buda, E. Chinello, B. Dam, V. Di Palma, T. Edvinsson, K. Fujii, H. Gardeniers, H. Geerlings, S. M. H. Hashemi, S. Haussener, F. Houle, J. Huskens, B. D. James, K. Konrad, A. Kudo, P. P. Kunturu, D. Lohse, B. Mei, E. L. Miller, G. F. Moore, J. Muller, K. L. Orchard, T. E. Rosser, F. H. Saadi, J.-W. Schüttauf, B. Seger, S. W. Sheehan, W. A. Smith, J. Spurgeon, M. H. Tang, R. van de Krol, P. C. K. Vesborg, P. Westerik, *Energy Environ. Sci.* **2018**, *11*, 2768.
[5] P. Quaino, F. Juarez, E. Santos, W. Schmickler, *Beilstein J. Nanotechnol.* **2014**, *5*, 846.
[6] D. Strmcnik, P. P. Lopes, B. Genorio, V. R. Stamenkovic, N. M. Markovic, *Nano Energy* **2016**, *29*, 29.
[7] U. Gupta, C. N. R. Rao, *Nano Energy* **2017**, *41*, 49.
[8] Q. Ding, B. Song, P. Xu, S. Jin, *Chem* **2016**, *1*, 699.
[9] Y. Xue, Q. Zhang, W. Wang, H. Cao, Q. Yang, L. Fu, *Adv. Energy Mater.* **2017**, *7*, 1.
[10] C. (Rose) Zhu, D. Gao, J. Ding, D. Chao, J. Wang, *Chem. Soc. Rev.* **2018**, *47*, 4332.
[11] D. Voiry, J. Yang, M. Chhowalla, *Adv. Mater.* **2016**, *28*, 6197.
[12] T. F. Jaramillo, K. P. Jørgensen, J. Bonde, J. H. Nielsen, S. Horch, I. Chorkendorff, *Science* **2007**, *317*, 100.
[13] B. Hinnemann, P. Moses, J. Bonde, K. P. Jørgensen, J. H. Nielsen, S. Horch, I. Chorkendorff, J. K. Nørskov, *J. Am. Chem. Soc.* **2005**, *127*, 5308.
[14] C. L. Bentley, M. Kang, F. Maddar, F. Li, M. Walker, J. Zhang, P. R. Unwin, *Chem. Sci.* **2017**, *8*, 6583.
[15] L. Gong, S. C. Haur, *J. Mater. Chem. C* **2017**, *5*, 2090.
[16] M. Ruhul Amin, M. Anower Hossain, Y. Zakaria, R. Amin, *ACS Appl. Mater. Interfaces* **2018**, *10*, 13509.
[17] R. Ding, Y. Liu, M. Wang, L. Qin, X. Cui, C. Wang, L. Wang, B. Lv, *Electrochim. Acta* **2017**, *248*, 20.
[18] X. Hai, W. Zhou, K. Chang, H. Pang, H. Liu, L. Shi, F. Ichihara, J. Ye, *J. Mater. Chem. A* **2017**, *5*, 8591.
[19] A. Y. Lu, X. Yang, C. C. Tseng, S. Min, S. H. Lin, C. L. Hsu, H. Li, H. Idriss, J. L. Kuo, K. W. Huang, L. J. Li, *Small* **2016**, *12*, 5530.
[20] R. N. Bhattacharya, C. Y. Lee, F. H. Pollak, D. M. Schleich, *J. Non-Cryst. Solids* **1987**, *91*, 235.
[21] D. Bélanger, G. Laperriere, B. Marsan, *J. Electroanal. Chem.* **1993**, *347*, 165.
[22] D. Merki, S. Fierro, H. Vrubel, X. Hu, *Chem. Sci.* **2011**, *2*, 1262.
[23] D. W. Redman, J. Kim, J. Stevenson, M. J. Rose, *J. Mater. Chem. A* **2016**, *4*, 7027.
[24] G. Q. Han, X. Shang, S. S. Lu, B. Dong, X. Li, Y. R. Liu, W. H. Hu, J. Bin Zeng, Y. M. Chai, C. G. Liu, *Int. J. Hydrogen Energy* **2017**, *42*, 5132.
[25] D. W. Redman, M. J. Rose, K. J. Stevenson, *Langmuir* **2017**, *33*, 9354.
[26] S. Murugesan, A. Akkineni, B. P. Chou, M. S. Glaz, D. A. Vanden Bout, K. J. Stevenson, *ACS Nano* **2013**, *7*, 8199.
[27] H. Vrubel, X. Hu, *ACS Catal.* **2013**, *3*, 2002.
[28] S. M. Tan, M. Pumera, *ACS Appl. Mater. Interfaces* **2017**, *9*, 41955.
[29] X. Chia, N. A. A. Sutrisnoh, M. Pumera, *ACS Appl. Mater. Interfaces* **2018**, *10*, 8702.
[30] D. Merki, H. Vrubel, L. Rovelli, S. Fierro, X. Hu, *Chem. Sci.* **2012**, *3*, 2515.
[31] M. Shang, H. Qi, C. Du, H. Huang, S. Wu, J. Zhang, W. Song, *Sens. Actuators, B* **2018**, *266*, 71.
[32] J. H. Kim, H. Kim, J. Kim, H. J. Lee, J. H. Jang, S. H. Ahn, *J. Power Sources* **2018**, *392*, 69.
[33] Z. Liu, X. Zhang, B. Wang, M. Xia, S. Gao, X. Liu, A. Zavabeti, J. Z. Ou, K. Kalantar-Zadeh, Y. Wang, *J. Phys. Chem. C* **2018**, *122*, 12589.
[34] F. Scaglione, Y. Xue, F. Celegato, P. Rizzi, L. Battezzati, *J. Mater. Sci.* **2018**, *53*, 12388.

[35] J. Tan, W. Yang, Y. Oh, H. Lee, J. Park, J. Moon, *ACS Appl. Mater. Interfaces* **2018**, *10*, 10898.
[36] Y. Li, K. Yin, L. Wang, X. Lu, Y. Zhang, Y. Liu, D. Yan, Y. Song, S. Luo, *Appl. Catal., B* **2018**, *239*, 537.
[37] H. Li, C. Tsai, A. L. Koh, L. Cai, A. W. Contryman, A. H. Fragapane, J. Zhao, H. S. Han, H. C. Manoharan, F. Abild-Pedersen, J. K. Nørskov, X. Zheng, *Nat. Mater.* **2016**, *15*, 48.
[38] C. C. Cheng, A. Y. Lu, C. C. Tseng, X. Yang, M. N. Hedhili, M. C. Chen, K. H. Wei, L. J. Li, *Nano Energy* **2016**, *30*, 846.
[39] G. Gao, Q. Sun, A. Du, *J. Phys. Chem. C* **2016**, *120*, 16761.
[40] Y. Ouyang, C. Ling, Q. Chen, Z. Wang, L. Shi, J. Wang, *Chem. Mater.* **2016**, *28*, 4390.
[41] J. P. Thiruraman, K. Fujisawa, G. Danda, P. M. Das, T. Zhang, A. Bolotsky, N. Perea-López, A. Nicolaï, P. Senet, M. Terrones, M. Drndić, *Nano Lett.* **2018**, *18*, 1651.
[42] C. Tsai, H. Li, S. Park, J. Park, H. S. Han, J. K. Nørskov, X. Zheng, F. Abild-Pedersen, *Nat. Commun.* **2017**, *8*, 15113.
[43] Y. Bao, M. Yang, S. J. R. Tan, Y. P. Liu, H. Xu, W. Liu, C. T. Nai, Y. P. Feng, J. Lu, K. P. Loh, *J. Am. Chem. Soc.* **2016**, *138*, 14121.
[44] G. Li, D. Zhang, Q. Qiao, Y. Yu, D. Peterson, A. Zafar, R. Kumar, S. Curtarolo, F. Hunte, S. Shannon, Y. Zhu, W. Yang, L. Cao, *J. Am. Chem. Soc.* **2016**, *138*, 16632.
[45] Y. Yin, J. Han, Y. Zhang, X. Zhang, P. Xu, Q. Yuan, L. Samad, X. Wang, Y. Wang, Z. Zhang, P. Zhang, X. Cao, B. Song, S. Jin, *J. Am. Chem. Soc.* **2016**, *138*, 7965.
[46] J. Xie, J. Zhang, S. Li, F. Grote, X. Zhang, H. Zhang, R. Wang, Y. Lei, B. Pan, Y. Xie, *J. Am. Chem. Soc.* **2013**, *135*, 17881.
[47] G. Ye, Y. Gong, J. Lin, B. Li, Y. He, S. T. Pantelides, W. Zhou, R. Vajtai, P. M. Ajayan, *Nano Lett.* **2016**, *16*, 1097.
[48] D. Escalera-López, R. Griffin, M. Isaacs, K. Wilson, R. E. Palmer, N. V. Rees, *Appl. Mater. Today* **2018**, *11*, 70.
[49] J. Hu, B. Huang, C. Zhang, Z. Wang, Y. An, D. Zhou, H. Lin, M. K. H. Leung, S. Yang, *Energy Environ. Sci.* **2017**, *10*, 593.
[50] S. M. Senthil Kumar, K. Selvakumar, J. Karthikeyan, R. Thangamuthu, P. Murugan, P. Rajput, S. N. Jha, D. Bhattacharyya, N. Navascues, S. Irusta, *ChemistrySelect* **2017**, *2*, 4667.
[51] L. Lin, N. Miao, Y. Wen, S. Zhang, P. Ghosez, Z. Sun, D. A. Allwood, *ACS Nano* **2016**, *10*, 8929.
[52] Z. Wang, Q. Li, H. Xu, C. Dahl-Petersen, Q. Yang, D. Cheng, D. Cao, F. Besenbacher, J. V. Lauritsen, S. Helveg, M. Dong, *Nano Energy* **2018**, *49*, 634.
[53] D. Escalera-López, Y. Niu, S. J. Park, M. Isaacs, K. Wilson, R. E. Palmer, N. V. Rees, *Appl. Catal., B* **2018**, *235*, 84.
[54] N. H. Attanayake, A. C. Thenuwara, A. Patra, Y. V. Aulin, T. M. Tran, H. Chakraborty, E. Borguet, M. L. Klein, J. P. Perdew, D. R. Strongin, *ACS Energy Lett.* **2018**, *3*, 7.
[55] A. Puntambekar, N. Chandrasekeran, Q. Wang, I. Roy, V. Premkumar, V. Chakrapani, *ACS Appl. Energy Mater.* **2018**, *1*, 3093.
[56] P. Liu, J. Zhu, J. Zhang, P. Xi, K. Tao, D. Gao, D. Xue, *ACS Energy Lett.* **2017**, *2*, 745.
[57] K. Qi, S. Yu, Q. Wang, W. Zhang, J. Fan, W. T. Zheng, X. Cui, *J. Mater. Chem. A* **2016**, *4*, 4025.
[58] Y. Shi, Y. Zhou, D.-R. Yang, W.-X. Xu, C. Wang, F.-B. Wang, J.-J. Xu, X.-H. Xia, H.-Y. Chen, *J. Am. Chem. Soc.* **2017**, *139*, 15479.
[59] J. Luxa, P. Vosecký, V. Mazánek, D. Sedmidubský, M. Pumera, Z. Sofer, *ACS Catal.* **2018**, *8*, 2774.
[60] D. Escalera-López, Y. Niu, J. Yin, K. Cooke, N. V. Rees, R. E. Palmer, *ACS Catal.* **2016**, *6*, 6008.
[61] T. H. M. Lau, X. Lu, J. Kulhavý, S. Wu, L. Lu, T.-S. Wu, R. Kato, J. S. Foord, Y.-L. Soo, K. Suenaga, S. C. E. Tsang, *Chem. Sci.* **2018**, *9*, 4769.
[62] Z. Luo, Y. Ouyang, H. Zhang, M. Xiao, J. Ge, Z. Jiang, J. Wang, D. Tang, X. Cao, C. Liu, W. Xing, *Nat. Commun.* **2018**, *9*, 1.
[63] P. Zhang, B. Xu, G. Chen, C. Gao, M. Gao, *Electrochim. Acta* **2018**, *270*, 256.
[64] J. Pan, C. Song, X. Wang, X. Yuan, Y. Fang, C. Guo, W. Zhao, F. Q. Huang, *Inorg. Chem. Front.* **2017**, *4*, 1895.
[65] C. Ray, S. C. Lee, K. V. Sankar, B. Jin, J. Lee, J. H. Park, S. C. Jun, *ACS Appl. Mater. Interfaces* **2017**, *9*, 37739.
[66] J. Li, J. Kang, Q. Cai, W. Hong, C. Jian, W. Liu, K. Banerjee, *Adv. Mater. Interfaces* **2017**, *4*, 1700303.
[67] T. Weber, J. C. Muijsers, J. W. Niemantsverdriet, *J. Phys. Chem.* **1995**, *99*, 9194.
[68] H. G. S. Casalongue, J. D. Benck, C. Tsai, R. K. B. Karlsson, S. Kaya, M. L. Ng, L. G. M. Pettersson, F. Abild-Pedersen, J. K. Nørskov, H. Ogasawara, T. F. Jaramillo, A. Nilsson, *J. Phys. Chem. C* **2014**, *118*, 29252.
[69] B. Lassalle-Kaiser, D. Merki, H. Vrubel, S. Gul, V. K. Yachandra, X. Hu, J. Yano, *J. Am. Chem. Soc.* **2015**, *137*, 314.
[70] Y. Deng, L. R. L. Ting, P. H. L. Neo, Y.-J. Zhang, A. A. Peterson, B. S. Yeo, *ACS Catal.* **2016**, *6*, 7790.
[71] P. D. Tran, T. V. Tran, M. Orio, S. Torelli, Q. D. Truong, K. Nayuki, Y. Sasaki, S. Y. Chiam, R. Yi, I. Honma, J. Barber, V. Artero, *Nat. Mater.* **2016**, *15*, 640.
[72] Y. Li, R. Nakamura, *Chin. J. Catal.* **2018**, *39*, 401.
[73] X. Chia, A. Ambrosi, D. Sedmidubský, Z. Sofer, M. Pumera, *Chem. – Eur. J.* **2014**, *20*, 17426.
[74] M. Zafir Mohamad Nasir, Z. Sofer, M. Pumera, *ChemElectroChem* **2015**, *2*, 1713.
[75] G. Li, D. Zhang, Y. Yu, S. Huang, W. Yang, L. Cao, *J. Am. Chem. Soc.* **2017**, *139*, 16194.
[76] H. Mishra, S. Umrao, J. Singh, R. K. Srivastava, R. Ali, A. Misra, A. Srivastava, *Adv. Opt. Mater.* **2017**, *5*, 1601021.
[77] N. Dubouis, C. Yang, R. Beer, L. Ries, D. Voiry, A. Grimaud, *ACS Catal.* **2018**, *8*, 828.
[78] L. R. L. Ting, Y. Deng, L. Ma, Y. J. Zhang, A. A. Peterson, B. S. Yeo, *ACS Catal.* **2016**, *6*, 861.
[79] J. Chandrasekaran, M. A. Ansari, S. Sarkar, *J. Less-Common Met.* **1987**, *134*, 23.
[80] Y. Yu, S. Y. Huang, Y. Li, S. N. Steinmann, W. Yang, L. Cao, *Nano Lett.* **2014**, *14*, 553.
[81] X.-Q. Bao, D. Y. Petrovykh, P. Alpuim, D. G. Stroppa, N. Guldris, H. Fonseca, M. Costa, J. Gaspar, C. Jin, L. Liu, *Nano Energy* **2015**, *16*, 130.
[82] M. Pourbaix, *Altas of Electrochemical Equilibrium in Aqueous Solutions*, Pergamon Press, New York **1966**.
[83] D. McAteer, Z. Gholamvand, N. McEvoy, A. Harvey, E. O'Malley, G. S. Duesberg, J. N. Coleman, *ACS Nano* **2016**, *10*, 672.
[84] Y. Li, Y. Yu, Y. Huang, R. A. Nielsen, W. A. Goddard, Y. Li, L. Cao, *ACS Catal.* **2015**, *5*, 448.
[85] L. A. Kibler, J. M. Hermann, A. Abdelrahman, A. A. El-Aziz, T. Jacob, *Curr. Opin. Electrochem.* **2018**, *9*, 265.
[86] L. A. Khanova, L. I. Krishtalik, *J. Electroanal. Chem.* **2011**, *660*, 224.
[87] A. Kahyarian, B. Brown, S. Nesic, *J. Electrochem. Soc.* **2017**, *164*, H365.
[88] T. Ohmori, M. Enyo, *Electrochim. Acta* **1992**, *37*, 2021.
[89] S. J. Rowley-Neale, D. A. C. Brownson, G. C. Smith, D. A. G. Sawtell, P. J. Kelly, C. E. Banks, *Nanoscale* **2015**, *7*, 18152.
[90] T. R. Hellstern, J. Kibsgaard, C. Tsai, D. W. Palm, L. A. King, F. Abild-Pedersen, T. F. Jaramillo, *ACS Catal.* **2017**, *7*, 7126.
[91] D. Kong, H. Wang, J. Cha, M. Pasta, K. Koski, *Nano Lett.* **2013**, *13*, 1341.
[92] I. Ledezma-Yanez, W. D. Z. Wallace, P. Sebastián-Pascual, V. Climent, J. M. Feliu, M. T. M. Koper, *Nat. Energy* **2017**, *2*, 1.
[93] T. Cheng, L. Wang, B. V. Merinov, W. A. Goddard, *J. Am. Chem. Soc.* **2018**, *140*, 7787.
[94] D. Strmcnik, M. Uchimura, C. Wang, R. Subbaraman, N. Danilovic, D. Van Der Vliet, A. P. Paulikas, V. R. Stamenkovic, N. M. Markovic, *Nat. Chem.* **2013**, *5*, 300.
[95] J. Zheng, W. Sheng, Z. Zhuang, B. Xu, Y. Yan, *Sci. Adv.* **2016**, *2*, e1501602.

[96] S. Haghighat, J. M. Dawlaty, *J. Phys. Chem. C* **2016**, *120*, 28489.
[97] N. Mohamad Latiff, L. Wang, C. C. Mayorga-Martinez, Z. Sofer, A. C. Fisher, M. Pumera, *Nanoscale* **2016**, *8*, 16752.
[98] J. Bonde, P. G. Moses, T. F. Jaramillo, J. Norskov, I. Chorkendorff, *Faraday Discuss.* **2008**, *140*, 219.
[99] D. N. Nguyen, L. N. Nguyen, P. D. Nguyen, T. V. Thu, A. D. Nguyen, P. D. Tran, *J. Phys. Chem. C* **2016**, *120*, 28789.
[100] X. Chia, A. Ambrosi, Z. Sofer, J. Luxa, M. Pumera, *ACS Nano* **2015**, *9*, 5164.
[101] V. S. Saji, C. W. Lee, *ChemSusChem* **2012**, *5*, 1146.
[102] J. C. Dupin, D. Gonbeau, I. Martin-Litas, P. Vinatier, A. Levasseur, *Appl. Surf. Sci.* **2001**, *173*, 140.
[103] G. C. Stevens, T. Edmonds, *J. Catal.* **1975**, *37*, 544.
[104] C.-H. Lee, S. Lee, Y.-K. Lee, Y. C. Jung, Y.-I. Ko, D. C. Lee, H.-I. Joh, *ACS Catal.* **2018**, *8*, 5221.
[105] P. C. K. Vesborg, B. Seger, I. Chorkendorff, *J. Phys. Chem. Lett.* **2015**, *6*, 951.
[106] M. Ledendecker, J. S. Mondschein, O. Kasian, S. Geiger, D. Göhl, M. Schalenbach, A. Zeradjanin, S. Cherevko, R. E. Schaak, K. Mayrhofer, *Angew. Chem., Int. Ed.* **2017**, *56*, 9767.
[107] C. C. L. McCrory, S. Jung, J. C. Peters, T. F. Jaramillo, *J. Am. Chem. Soc.* **2013**, *135*, 16977.
[108] C. Spöri, J. T. H. Kwan, A. Bonakdarpour, D. P. Wilkinson, P. Strasser, *Angew. Chem., Int. Ed.* **2017**, *56*, 5994.
[109] J. D. Benck, T. R. Hellstern, J. Kibsgaard, P. Chakthranont, T. F. Jaramillo, *ACS Catal.* **2014**, *4*, 3957.
[110] N. Q. Tran, V. Q. Bui, H. M. Le, Y. Kawazoe, H. Lee, *Adv. Energy Mater.* **2018**, *8*, 1702139.
[111] Y. Sun, C. Liu, D. C. Grauer, J. Yano, J. R. Long, P. Yang, C. J. Chang, *J. Am. Chem. Soc.* **2013**, *135*, 17699.
[112] H. W. Wang, P. Skeldon, G. E. Thompson, *Surf. Coat. Technol.* **1997**, *91*, 200.
[113] W. Grunert, A. Y. Stakheev, R. Feldhaus, K. Anders, E. S. Shpiro, K. M. Minachev, *J. Phys. Chem.* **1991**, *95*, 1323.